Large Eddy Simulations of Alternative Jet Fuel Combustion

Åkerblom, Arvid

2025

Document Version:
Publisher's PDF, also known as Version of record

Large Eddy Simulations of Alternative Jet Fuel Combustion

ARVID ÅKERBLOM
DEPARTMENT OF ENERGY SCIENCES | FACULTY OF ENGINEERING | LUND UNIVERSITY

Printed by Media-Tryck, Lund 2025
NORDIC SWAN ECOLABEL 3041 0903

LUND UNIVERSITY

Faculty of Engineering
Department of Energy Sciences
Division of Heat Transfer

ISBN 978-91-8104-505-5
ISSN 0280-1990
ISRN LUTMDN/TMHP-25/1180-SE

Large Eddy Simulations of Alternative Jet Fuel Combustion

Large Eddy Simulations of Alternative Jet Fuel Combustion

by Arvid Åkerblom

LUND
UNIVERSITY

Thesis for the degree of Doctor of Philosophy
Thesis advisors: Prof. Christer Fureby, Associate Prof. Elna Heimdal Nilsson
Faculty opponent: Prof. Andreas Kempf

To be presented, with the permission of the Faculty of Engineering of Lund University, for public criticism in Room E:B on Thursday the 12th of June 2025 at 10:15.

Organization
LUND UNIVERSITY

Department of Energy Sciences
Box 118
SE–221 00 LUND
Sweden

Document name
DOCTORAL DISSERTATION

Date of disputation
2025-06-12

Sponsoring organization

Author(s)
Arvid Åkerblom

Title and subtitle
Large Eddy Simulations of Alternative Jet Fuel Combustion

Abstract
Sustainable Aviation Fuels (SAF) are the most promising strategy for reducing the carbon emissions of aviation in the near term, but their combustion behavior is not well understood compared to conventional fuels. This work investigates how different properties of SAF may lead to different emergent combustion behavior by targeting a small set of very distinct fuels. The investigation is carried out numerically using reactive Large Eddy Simulations (LES) and Finite Rate Chemistry (FRC), incorporating the effects of turbulence as well as crucial chemical differences between the fuels. Two cases are studied: a simple premixed bluff body flame and a generic aeroengine-like spray combustor operated at idle and cruise conditions. The targeted fuels include conventional Jet A, a pure alcohol-to-jet SAF called C1, and an aromatics-heavy test fuel called C5. A set of correlations is developed to capture the liquid properties of these fuels across all relevant temperatures. Combustion chemistry is modeled using two sets of pathway-centric reaction mechanisms that are detailed enough to differentiate between fuels. All simulations are validated against available experimental data and show good agreement.

The results reveal several distinct fuel trends. In premixed flames, the size of the flame sheet is correlated with the flame temperature. Different fuels experience different levels of flame surface fluctuations, which are found to be correlated with Cetane number. A novel flame-dampening mechanism is proposed to explain this connection.

In spray flames, the fuels behave similarly to each other at idle conditions, where premixed burning dominates. The spray length and emission profile of each fuel is demonstrably determined by its vaporizability and hydrogen/carbon ratio, respectively. At cruise conditions, where there is less premixing, new trends emerge. The more volatile fuels C1 and C5 have more compact flames than Jet A; this causes them to burn at a higher equivalence ratio, increasing NO_x emissions. C1 and C5 also experience stronger thermoacoustic fluctuations, which is likely caused by their high vaporizability but may also be linked to their low Cetane numbers relative to Jet A.

Key words
Computational Fluid Dynamics, Large Eddy Simulation, Sustainable Aviation Fuel, Jet Engine, Turbulent Combustion

Classification system and/or index terms (if any)

Supplementary bibliographical information

Language
English

ISSN and key title
ISSN: 0280-1990
ISRN: LUTMDN/TMHP-25/1180-SE

ISBN
978-91-8104-505-5 (print)
978-91-8104-506-2 (pdf)

Recipient's notes

Number of pages
231

Price

Security classification

Large Eddy Simulations of Alternative Jet Fuel Combustion

by Arvid Åkerblom

LUND
UNIVERSITY

A doctoral thesis at a university in Sweden takes either the form of a single, cohesive research study (monograph) or a summary of research papers (compilation thesis), which the doctoral student has written alone or together with one or several other author(s).

In the latter case the thesis consists of two parts. An introductory text puts the research work into context and summarizes the main points of the papers. Then, the research publications themselves are reproduced, together with a description of the individual contributions of the authors. The research papers may either have been already published or are manuscripts at various stages (in press, submitted, or in draft).

Cover illustration: A team of brilliant minds at the cutting edge of combustion squience. By Moa Åkerblom.

Funding information: This work was funded by the European Union's Horizon 2020 research and innovation program MORE&LESS under grant agreement no. 769246, with additional support from the competence center CESTAP funded by the Swedish Energy Agency under grant agreement no. 52683-1. Computational resources were provided by the Swedish National Infrastructure for Computing (SNIC), partially funded by the Swedish Research Council through grant agreement no. 2018-05973. Further computational resources were provided by the National Academic Infrastructure for Supercomputing in Sweden (NAISS), partially funded by the Swedish Research Council through grant agreement no. 2022-06725.

Division of Heat Transfer
Department of Energy Sciences
Faculty of Engineering
Box 118
SE 221-00 Lund
Sweden

ISBN: 978-91-8104-505-5 (print)
ISBN: 978-91-8104-506-2 (pdf)
ISSN: 0280-1990
ISRN: LUTMDN/TMHP-25/1180-SE

Printed in Sweden by Media-Tryck, Lund University, Lund 2025

To Olle Bergman

Contents

Publications included in the thesis

This thesis is based on the following publications, referred to by their Roman numerals:

I **Large Eddy Simulations of Turbulent Premixed Bluff Body Flames Operated with Ethanol, n-Heptane, and Jet Fuels**
A. Åkerblom & C. Fureby
Combustion and Flame, 272:113895, 2025.

II **Comparing Chemical Reaction Mechanisms for Jet Fuel in Turbulent Premixed Combustion Simulations**
A. Åkerblom, N. Zettervall & C. Fureby
AIAA Journal, 2025. In press.

III **LES Modeling of the DLR Generic Single-Cup Spray Combustor: Validation and the Impact of Combustion Chemistry**
A. Åkerblom & C. Fureby
Flow, Turbulence and Combustion, 112:557–585, 2024.

IV **Numerical Modeling of Chemical Kinetics, Spray Dynamics, and Turbulent Combustion Towards Sustainable Aviation**
A. Åkerblom, M. Passad, A. Ercole, N. Zettervall, E.J.K. Nilsson & C. Fureby
Aerospace, 11:31, 2024.

V **LES Modeling of the DLR Generic Single-Cup Spray Combustor: Comparison of Exploratory Category C Jet Fuels**
A. Åkerblom & C. Fureby
Flow, Turbulence and Combustion, 2025. [Advance online publication]. Available at: https://doi.org/10.1007/s10494-025-00653-8

Publications not included in the thesis

i **Numerical Simulations of Spray Combustion in Jet Engines**

A. Åkerblom, F. Pignatelli & C. Fureby
Aerospace, 9:838, 2022.

ii **The Impact of Reaction Mechanism Complexity in LES of Liquid Kerosene Spray Combustion**
A. Åkerblom
In *Proceedings of the 33rd Congress of the International Council of the Aeronautical Sciences*, Stockholm, Sweden, 4–9 September, 2022.

iii **Predictions of Spray Combustion using Conventional Category A Fuels and Exploratory Category C Fuels**
F. Pignatelli, M. Passad, **A. Åkerblom**, T. Nilsson, E.J.K. Nilsson & Christer Fureby
In *Proceedings of the AIAA SciTech 2023 Forum*, National Harbor, 23–27 January, 2023. AIAA 2023-1486.

iv **Comparing Chemical Reaction Mechanisms for Jet Fuel Combustion in Simulations of a Turbulent Premixed Bluff-Body Burner**
A. Åkerblom, N. Zettervall & C. Fureby
In *Proceedings of the AIAA SciTech 2024 Forum*, Orlando, 8–12 January, 2024. AIAA 2024-0179.

v **Multidimensional Chemistry Coordinate Mapping for Large Eddy Simulations of a Turbulent Premixed Bluff-Body Burner**
P. Vauquelin, Y. Zhou, **A. Åkerblom**, C. Fureby & X.-S. Bai
In *Proceedings of the AIAA SciTech 2025 Forum*, Orlando, 6–10 January, 2025. AIAA 2025-2485.

Acknowledgements

This thesis is the culmination of four and a half years of work, starting with my MSc project in January 2021, which later transitioned into a PhD. Looking back at my early simulations and texts, I feel some embarrassment (they are, frankly, not great), but also pride: pride in my growth as a scientist and person since then, pride in the final products of the work, and pride in my determination to see it through to the end. But I know that I never would have come so far without the support of my colleagues, friends, and family. It is impossible for me to fully articulate my gratitude in this short section, but I will try my best.

First, I would like to thank my main supervisor Christer Fureby. Your expertise with LES, combustion simulations, and OpenFOAM allowed me to dive straight into my research; without it, I would easily have spent the first two years just figuring out how to run a proper simulation. More importantly, however, I appreciate the faith you have consistently placed in me and my abilities over the years. You have pushed me to strive for more because you were confident I could do it. In cases where I couldn't do it, you accepted that it was due to unforeseen challenges and not a personal failure. You also gave me the freedom to pursue my own goals and write my papers as I saw fit. Every PhD student is different, but to me, this was the ideal form of supervision, and you understood that early on.

I also wish to thank my assistant supervisor Elna Heimdal Nilsson and my PhD colleague Martin Passad over at Combustion Physics. We spoke frequently during the early stages of my PhD, and the knowledge you gave me on fuel chemistry and chemical kinetics proved invaluable later on. Combustion Physics is a hoot, by the way - Megha, Mattias, David, thanks for all the fun conversations.

Niklas Zettervall, thank you for two great collaborations on papers II and IV. Your reaction mechanisms are the future of jet fuel combustion in CFD. See you at FOI!

Now for the Division of Heat Transfer, my home for the last four years. All the little conversations and exchanges of ideas that we had here over the years helped my research become so much more, and I hope that goes for the rest of you as well. Let me start with my past and present "roommates". Yuxiang: I could not have asked for a gentler and more enthusiastic companion as we waded through the mire of crashing simulations and harsh reviewers. Gustav, thanks for all the intense 7 Wonders games; I don't remember our scoreboard, but know that I will kick your ass next time we sit down to play. Heng, I wish you the best of luck for the remainder of your project. As for my "neighbors": Bora, thanks for all the deep and insightful conversations (and the whiskey). Alessandro, you are probably the sharpest guy I have ever met, and I can't wait to see where your research takes you. Rasmus, I can only wish that I had your attention to detail and eagerness to get to the bottom of physics and code. Shuo, thanks for the dance at EFMC14. Danan, thanks for being my "thesis buddy" for these last few months. Björn, you did a brilliant job during

your MSc project, and I am glad to have you on the case with thermoacoustics, a topic my own feeble mind was only able to scratch the surface of. Pierre V, your accomplishments with CCM and CHT in just your first year make me feel like a fossil by comparison - I hope I have time to grill you on some of this stuff so I can bring my own simulations out of the stone age. Jan-Peter, thanks for helping me understand jet engines, which I should have probably gotten around to by myself by my fourth year. Himani, speaking to you is always a pleasure - it's just a shame our Swedish and Indian lunch schedules clash so hard. Thommie, I still feel some lingering existential dread from when you gave a seminar questioning the fundamental concept of a mesh cell. Diamantis, Marcus, Mattias, Christian, Xin, Pierre DR, Pamella, Rania, and Amey, thanks for making Heat Transfer what it is, and good luck in your projects!

My co-teachers in the thermodynamics course, Christoffer and Lei: you are both inspiring lecturers, and teaching alongside you allowed me to actually learn thermodynamics (unlike during my undergrad, when I somehow scraped by anyway). Martin and Thommie: thanks for several years of quality teaching in the energy markets course. Perhaps this is the time to mention that literally all my knowledge about energy markets is confined to the two reports I used as sources?

As for the rest of the Dept. of Energy Sciences, thank you for all the barbecues, after works, and pleasant lunches. When I started in 2021, the COVID-19 pandemic was still raging, and the social life among junior researchers was practically non-existent. It slowly started up again in 2022 and 2023, but it wasn't until we got some new blood in 2024 that the PhD community became really vibrant. It's a joy to see. Miaoxin, Francesco, Alexandra, Peter, Yannick, Beyza, Anupam, Carl-Otto, Mirjam, Margherita, Federico, Christoffer, Luis, Axel, and the rest: I am glad to have crossed paths with you all.

To my wife, Moa: thank you for the endless support and understanding you have given me during these years. You helped me keep my feet on the ground when things felt overwhelming. You made sure I always had access to a steady supply of hugs when I had to revise papers and re-run simulations. And of course, thank you for the stellar thesis cover!

Finally, I want to thank my families Åkerblom and Bergman. My father Per, whose endless curiosity about the workings of the world rubbed off on me and is the reason I chose to pursue science. My mother Ina, whose determination to see things through has always inspired me. My brother John, whom I admire for his grit and ability to stake his own path. My in-laws Lotten, Erik, Ida, Julian, Oskar, Sigge, Freja, Matilda, and Alva, who have wholeheartedly welcomed me into their family and always shown an interest in what I do. My sister-in-law Frida, proofreader extraordinaire, who inspired me to become a PhD student in the first place. Lastly, my father-in-law Olle, to whom this thesis is dedicated: you were a living embodiment of the whimsy in science, and I wish you were still here.

Popular summary in English

The aviation industry releases 2.5% of global CO_2 emissions and is a major contributor to climate change. Reducing these emissions is challenging due to the design requirements placed on aircraft engines: electric motors and fuel cells are too heavy for larger aircraft, while hydrogen-burning jet engines are difficult to implement safely and reliably. However, there is hope in the form of Sustainable Aviation Fuel (SAF), i.e., renewable biofuels that can be used in conventional jet engines.

SAF can be produced in many ways. Some methods synthesize it from alcohol and sugar. Others use waste products like sewage or used cooking oil, giving the fuel a very low environmental footprint. Others still use biological byproducts from industrial processes; important examples of this in Sweden include forest residues or byproducts from paper production. The fuels produced by this wide range of methods and materials can vary greatly in composition and lack some important features of established fossil fuels. A general trend is a lack of aromatics, carbon rings that are naturally plentiful in petroleum and fossil fuels, which are necessary for proper lubrication and seal swelling in jet engines. For these reasons, SAF is only certified for use in aircraft when blended with fossil fuels up to a maximum ratio of 50/50.

When more than 50% SAF is put into the tank, the differences between it and conventional fuel can start to become noticeable. However, the effects of these differences are not well known because our scientific and practical experience burning SAF is minuscule compared to fossil fuels. There is an urgent need for research on how SAFs burn so that blending limits can be increased and new production methods can be certified. To gain as much knowledge as possible, it should not only be done with traditional experiments but also with detailed computer simulations. Simulations can provide data that is unobtainable using experimental measurements and allow for predictive and exploratory studies that generate new theories. Large Eddy Simulations (LES) are one such simulation technique, well-suited for studying the complex and turbulent combustion inside a jet engine, as it constructs a full 3D model of the constantly shifting flame. Although powerful, LES requires an astronomical amount of calculations, which makes access to a supercomputer a necessity.

This work uses LES to study the combustion of several jet fuels, including SAF. The set of fuels represents a wide range of characteristic properties like density and aromatics content, and each fuel is used in its pure form. In this way, the effects of the different properties become as impactful and measurable as possible, making it easier to connect them to the different combustion behaviors of each fuel. Two different cases are studied. Case A is a simple lab-scale burner, somewhat similar to a camping stove, where the fuel is fully vaporized and mixed with air before igniting. Case B is a generic model of a real jet engine combustor and includes many features of real engines, such as air pressures up to ten at-

mospheres, direct injection of liquid fuel into the combustion chamber, and swirlers that induce rotation in the flow to stabilize the flame. Both cases have previously been used in experiments elsewhere, and their results are publicly available. The LES model reproduces the available results very well, indicating that the modeling methodology is well-suited to the problem.

In case A, the simulations reveal several distinct fuel trends. The temperature at which each fuel burns decides the overall size of its flame, which is very useful information since the flame temperature can be easily calculated without either experiments or simulations. The ignition quality of each fuel, which is measured using the Cetane Number (CN), appears to influence how steady the flame is, with low-CN fuels having steadier flames than high-CN fuels. A hypothetical explanation for this unexpected result is formulated using chemical time scales, and further research will show how well it holds up.

In case B, the simulations show that the different fuels behave quite similarly when the engine is run in idle mode, but distinct differences emerge in cruise mode. The most important factor is the vaporizability, which is a measure of how easily the liquid fuel is broken up into small droplets and then turned into vapor. The more vaporizable fuels have more compact flames and burn closer to the fuel injector. This increases the fuel-to-air ratio where the chemical reactions happen, which in turn increases the flame temperature. Because the flame temperature is so high, the nitrogen in the air reacts with the oxygen to form nitrogen oxides, NO_x, which are harmful to both people and the environment. The more vaporizable fuels also give rise to strong pressure waves that make their flames less stable and put the engine under stress.

The combined results of this work demonstrate how radically different fundamental fuel properties lead to different combustion behaviors. As more experiments and simulation studies are carried out, the range of possible SAF properties and their effects will be mapped out and understood. This understanding should pave the way for higher blending limits with some SAFs and allow new production methods to enter the market.

Populärvetenskaplig sammanfattning på svenska

Flygindustrin står för 2.5% av de globala koldioxidutsläppen och bidrar betydligt till världens klimatförändringar. Att minska dessa utsläpp är särskilt svårt på grund av kraven som ställs på flygmotorer: elmotorer och bränsleceller är för tunga för större flygplan och väteförbränningsmotorer är svåra att implementera på ett säkert och tillförlitligt sätt. Därför är den mest lovande lösningen förnybart biobränsle som kan användas i existerande motorer, s.k. Sustainable Aviation Fuel (SAF).

SAF kan produceras på många sätt. Det finns metoder som syntetiserar det från alkohol och socker medan andra använder avfall som avloppsvatten och gammal matlagningsolja, vilket ger bränslet ett väldigt litet klimatavtryck. Det finns också metoder som använder biologiska restprodukter som är vanliga i Sverige, t.ex skogsavfällningar och rester från papperstillverkning. Bränslen som framställs via detta breda spann av metoder och råmaterial kan variera mycket i kemisk uppsättning och sakna vissa viktiga egenskaper som etablerade fossila bränslen har. Ett exempel är att SAF typiskt saknar aromater, kolringar som förekommer naturligt i råolja och fossila bränslen och som behövs för smörjning och packningssvällning i motorns bränslesystem. Av dessa skäl är SAF bara certifierat för användning efter att det har blandats ut med ett fossilt bränsle upp till en blandning på 50/50.

När mer än 50% av tanken innehåller SAF kan skillnaderna gentemot fossila bränslen visa sig. Effekterna av dessa skillnader är dock inte välkända eftersom vår vetenskapliga och praktiska erfarenhet med SAF är minimal jämfört med fossila bränslen. Det finns ett akut behov av forskning om hur SAF brinner så att inblandningsgränserna kan höjas och nya bränslen kan certifieras. För att generera så mycket kunskap som möjligt bör denna forskning ske både med traditionella experiment och med detaljerade datorsimuleringar. Simuleringar ger data som inte finns att tillgå från fysiska mätningar och tillåter utforskande studier som kan forma nya teorier. Large Eddy Simulations (LES) är en simuleringsteknik som är välanpassad för studier av den komplexa och turbulenta förbränningen i flygmotorer eftersom den konstruerar en rörlig 3D-modell av flamman. LES är en kraftfull metod som involverar astronomiska mängder uträkningar, vilket gör tillgång till en superdator till ett måste.

Detta verk använder LES för att undersöka förbränningen av flera flygbränslen, inkl. SAF. Dessa bränslen uppvisar ett brett spann av karakteristiska egenskaper såsom densitet och aromathalt och varje bränsle används i sin rena form. På detta vis träder bränslenas olika egenskaper tydligt fram, vilket gör det möjligt att koppla dem till varje bränsles förbränningsbeteende. Två olika fall undersöks. Fall A är en liten och enkel brännare, inte helt olik ett campingkök, med förångat bränsle som är fullständigt blandat med den omgivande luften innan det antänds. Fall B är en generisk modell av en verklig flygmotorbrännare och har mycket gemensamt med riktiga motorer, såsom lufttryck upp till tio atmosfärer, direkt injektion av vätskeformigt bränsle och virvlare som roterar luftflödet för att stabilisera flam-

man. Bägge fall har tidigare använts i experiment av andra grupper och resultaten från dessa är publicerade. LES-modellen återskapar dessa resultat väldigt väl, vilket demonstrerar att metodiken är välanpassad för problemet.

I fall A avslöjar simuleringarna flera tydliga bränsletrender. Temperaturen som varje bränsle brinner vid bestämmer den övergripande storleken på dess flamma, vilket är användbart eftersom temperaturen kan räknas ut på förhand. Antändningkvaliteten, som brukar mätas i cetan-tal (CN), verkar påverka flammans stabilitet så att bränslen med lägre CN brinner stabilare än bränslen med högre CN. Denna oväntade trend förklaras med hjälp av ett hypotetiskt samband mellan olika kemiska tidsskalor, och uppföljande forskning kommer att visa huruvida detta samband håller generellt.

I fall B visar simuleringarna att bränslena liknar varandra under tomgångskörning, medan betydande skillnader framträder vid kryssning. Den viktigaste faktorn är ångbildningsbenägenheten, alltså hur enkelt bränslet bildar små vätskedroppar och sedan förångas. Ju mer benägna bränslena är att övergå i gasform, desto kompaktare blir flammorna samtidigt som de rör sig närmare bränsleinjektorn. Detta ökar bränslehalten i luften där reaktionerna sker, vilket i sin tur höjer flamtemperaturen. Denna höga temperatur orsakar reaktioner mellan kvävet och syret i luften som bilder kväveoxider, NO_x, som är skadliga för både människor och miljön. Dessa bränslen ger även upphov till starka stående tryckvågor som gör flammorna mindre stabila och sliter på motorn.

De sammanlagda resultaten från detta verk demonstrerar hur radikalt olika bränsleegenskaper leder till olika förbränningsbeteenden. Allt eftersom fler experimentella och simuleringsbaserade studier utförs kommer spektrat av möjliga SAF-egenskaper och deras effekter att kartläggas och förstås. Denna kunskap bör bana vägen för ökad SAF-inblandning och nya produktionsmetoder.

List of important abbreviations

ATJ	Alcohol-To-Jet
CFD	Computational Fluid Dynamics
CN	Cetane Number
CRZ	Central Recirculation Zone
EI	Emission Index
FAR	Fuel-to-Air Ratio
FRC	Finite Rate Chemistry
FVM	Finite Volume Method
HHV	Higher Heating Value
HRR	Heat Release Rate
LES	Large Eddy Simulation
LHV	Lower Heating Value
MW	Molecular Weight
NTC	Negative Temperature Coefficient
ODE	Ordinary Differential Equation
ORZ	Outer Recirculation Zone
PaSR	Partially Stirred Reactor
PDE	Partial Differential Equation
PDF	Probability Density Function
PLIF	Planar Laser-Induced Fluorescence
RZ	Recirculation Zone
SAF	Sustainable Aviation Fuel
SMD	Sauter Mean Diameter
TCI	Turbulence-Chemistry Interaction
TR	Temperature Ratio

Chapter 1

Introduction

Over the last 120 years, the dream of flying has been turned from a dream to a reality, then an industry - a notoriously carbon-intensive industry. In 2019, aircraft released 1,000,000,000 tons of CO_2 into the atmosphere, representing 2.5% of global CO_2 emissions. Aviation also impacts the climate in other ways, such as forming contrails in the upper troposphere that affect the planet's radiation balance. Accounting for all known effects, aviation has contributed around 4% to global warming over time. These numbers are quite high, considering that only around 10% of humans fly most years. As more nations industrialize and the global standard of living rises, the demand for air travel will increase steadily and the carbon emissions of aviation will continue to grow, [1].

Three factors make aviation particularly difficult to decarbonize compared to other transport industries: weight, volume, and safety. The energy per unit mass and volume is much lower in batteries and fuel cells than in liquid fuels, forcing aircraft to devote much more of their weight and volume to the propulsion system, which leaves less room for passengers and cargo. As a result, batteries and fuel cells are limited to small, short-range aircraft. Although combustion engines are required for larger aircraft, the industry can still be decarbonized by replacing fossil fuels with carbon-neutral alternative fuels. However, the requirements placed on these must be quite strict to ensure safety. For modern cars and ships, engine failure is a moderately dangerous inconvenience; for aircraft, it is a catastrophe. For this reason, new fuels must either conform to existing fuel specifications, which rules out certain fuels and may increase production costs, or be used solely in specially designed engines that can take decades to develop and certify.

Although not covered in this thesis, hydrogen has a very high energy content per unit mass and combustion engines powered by sustainably sourced hydrogen are a promising solution for the future. However, compressing hydrogen to a useful density requires very

high pressures, and its combustion characteristics are dramatically different from those of conventional liquid hydrocarbon fuels. Entirely new propulsion systems must be developed for hydrogen, and the decarbonizing effect is contingent on the existence of a steady supply of sustainable hydrogen.

Sustainable Aviation Fuels (SAF) are liquid hydrocarbon fuels produced from renewable biomass. Depending on their composition, SAFs can fulfill all the specifications for conventional jet fuel, which means that they can be used in existing engines. If they do not, they can still be blended with conventional fuel until the product meets the requirements; such SAFs are referred to as drop-in fuels. The advantage of being able to use SAF in existing engines should not be understated: the International Aviation Transport Association (IATA) has estimated SAF to be the single biggest contributor to net zero CO_2 emissions by 2050, accounting for 65% of the total reduction. Of the remaining 35%, 19 are estimated to come from offsets and carbon capture, whereas 13 are associated with new propulsion technologies such as hydrogen engines, [2]. All SAFs are considered alternative jet fuels, i.e., they are not produced by the conventional process of petroleum refinement. The terms SAF and alternative jet fuel are nearly interchangeable, but alternative jet fuels do not have to be sustainably produced.

SAF comes in many varieties. The International Civil Aviation Organization (ICAO) lists 11 approved production methods, which use different types of raw material (a.k.a. feedstock) and result in different products. Important examples include Fischer-Tropsch (FT) fuels produced by gasification, Hydroprocessed Esters and Fatty Acids (HEFA) and Catalytic Hydrothermolysis (CHJ) fuels produced by refining oily biomass, and Alcohol-To-Jet (ATJ) fuels derived from alcohols, [3]. These fuels represent a broad spectrum of product properties, which can also vary from batch to batch depending on the specific feedstock used. A common denominator is a lack of aromatics (carbon-heavy cyclic hydrocarbons), which occur naturally in petroleum and are present in all conventional jet fuels. Because aromatics are low in energy and prone to form soot when burned, the lack of aromatics in SAF is in some ways an advantage. However, the key selling point of SAF is that it should be compatible with aircraft fuel systems, which contain elastomer seals that are designed to swell in the presence of aromatics. A minimum aromatics content of 8% (by volume) is therefore mandated for jet fuels, [4]. This, combined with the variability of properties and a lack of long-term experience, means that all SAF types are still used as drop-in fuels with a maximum blending ratio of 50% (or lower, for some types).

1.1 Motivation

Even with current blending limits, the carbon savings would be immense if aircraft were to consistently fly with close to 50% SAF in the tank. Unfortunately, this is still far from

becoming a reality: in 2023, SAF only accounted for 0.2% of global jet fuel consumption, [5]. Serious challenges include securing a reliable source of feedstock and lowering production costs to competitive levels. Scientific research into such techno-economic questions is extremely valuable and produces tangible benefits here and now. Studying the technical challenges of burning SAF above the blending limit, which is the topic of this thesis, is not as immediately beneficial but will become increasingly relevant over time. This kind of research has other benefits, however. By studying the combustion behavior of different fuels along the broad spectrum of SAF properties, we can gauge the impact of certain properties compared to others. Such knowledge can help drive the certification of new SAF production methods and adapt jet fuel specifications to a market with more SAF. It also furthers our understanding of the behavior of drop-in fuels - even if a 20/80 SAF/fossil blend falls well within the specifications of conventional jet fuel, its performance and emissions should lie somewhere between those of pure fossil fuel and pure SAF, and may be predicted by studying both extremes.

1.2 Knowledge gap

Fossil jet fuels are extremely complex on a chemical level, containing hundreds of different hydrocarbons of different types and sizes. Despite this, we are able to predict their combustion behavior quite accurately thanks to decades of research and experience. For SAF, research is still in its infancy, and many questions remain fully or partially unexplored. The following is a non-exhaustive list of such inquiries:

- How does burning different types of SAF in different conventional engines affect thrust and emissions?
- Are there any long-term effects on an engine caused by regularly burning SAF?
- How can future engines be adapted or optimized for SAF?
- How does the chemical composition of SAF affect the stability of the flame and its chance of blowing out?
- What makes a SAF easy or difficult to re-ignite?
- Is SAF more or less prone to triggering thermoacoustic instabilities in the engine?
- How do the distillation curve and other liquid properties of a SAF affect its combustion? When is this more or less relevant?
- How do the gas-phase kinetics of a SAF affect its combustion? When is this more or less relevant?

- To what extent can the fundamental properties of a SAF be used to predict its combustion behavior? Are there any nearly universal principles, or is everything heavily case-dependent?
- How reliable are established simulation models for predicting the combustion behavior of SAF? Where are the biggest uncertainties, and can they be reduced?

Each of the questions above requires many separate studies to answer adequately. These answers can (and should) come from two separate sources: experiments and numerical simulations. Experiments form the backbone of any engineering science but are often limited in the amount of information they can provide. Working with real jet engines is undoubtedly relevant, but they must typically be treated as semi-black boxes since instruments cannot easily be placed inside the combustion chamber during operation. Lab-scale test rigs are much more amenable to research, but even then, making quantitative measurements on a highly turbulent and chemically complex jet fuel flame may not be possible, especially in three spatial dimensions. Computer-aided numerical simulations do not have these limitations, providing full information about the flow, chemistry, and thermodynamics at all points in time and space within the simulated domain. On the other hand, simulations are limited by the many assumptions they must rely on, either due to a general lack of accurate models or due to limited computational power. Simulations shine when they are validated against experimental measurements; if the experimental observations are faithfully reproduced, the simulations can be used to visualize, analyze, and understand the underlying phenomena causing the observed effects. New hypotheses can then be formed, leading to new experiments and simulations in a continuous cycle of discovery.

There are many ways to simulate a combustion process depending on what type of results is desired. One strategy is Large Eddy Simulations (LES), [6], which involve solving the governing equations for flow and chemistry in both time and 3D space, allowing the flow and flame to develop in a way analogous to reality. LES is a category of Computational Fluid Dynamics (CFD) simulations, and the keyword "large" symbolizes that the smallest length and time scales of the flow are not simulated directly but instead represented by simpler models that aim to account for their influence on the larger flow structures. LES of reactive flows is computationally expensive and typically requires the use of high-performance computing. Thanks to advances in computational power, it has only recently become possible to combine LES with semi-detailed chemistry models that meaningfully distinguish between different types of fuels.

1.3 Aim and scope

This thesis describes LES of jet fuel combustion with the purpose of exploring how the composition and fundamental characteristics of jet fuels affect their turbulent combustion behavior. The simulations are carried out across two cases obtained from the literature: case A, a simple premixed bluff body burner useful for validating models and studying the fundamental flame dynamics, [7], and case B, a lab-scale spray combustor designed to represent the core of a real jet engine, [8]. Two pure alternative jet fuels are modeled: one representing a real commercial SAF (C1) and the other a test fuel with a very high aromatics content and flat boiling curve (C5). These are compared with the conventional civilian jet fuel Jet A and partly with the military jet fuel JP-5. Together, these fuels represent a broad range of properties in terms of liquid thermodynamics and gas-phase kinetics. The results are analyzed in multiple ways, ranging from simple comparisons of the velocity, temperature, and species concentrations to more advanced statistical methods like flame surface density. The primary objectives are as follows:

- To validate the chosen simulation method against experimental data, identifying its capabilities and limitations.
- To investigate the sensitivity of the simulations to mesh resolution and model choice.
- To identify differences in the combustion and emissions of the fuels and make informed hypotheses to explain them.
- To check whether there are any identifiable correlations between the fundamental gas-phase kinetics or liquid properties of the fuels and their turbulent combustion behavior.

To limit the scope, this work focuses solely on the combustion process itself and does not address its impact on the engine or aircraft as a whole. Blowout and re-ignition are likewise not considered. The simulation methodology is thoroughly validated against experimental data to ensure that the results are suitable for analysis, but the methodology itself is not novel. Moreover, due to the computational cost of the simulations and the substantial amount of work required to make them function as intended, the number of fuels and operating conditions is too small to make generalized conclusions with statistical certainty. The conclusions should instead be viewed as well-informed hypotheses to guide future work, while the results contribute to a growing body of data in the literature.

The LES methodology used here, although quite powerful for modeling the dynamics of turbulent combustion, is relatively simple in its predictions of emissions. The formation of nitrogen oxides (NO_x) is not modeled directly but obtained via post-processing. Particulate matter and unburnt hydrocarbons are not modeled. Radiative and conjugate heat

transfer are also deliberately neglected despite having a potentially substantial influence on the combustion process; this is done to limit the number of factors influencing the results, giving more weight to the thermochemical differences between the fuels.

1.4 Structure

The thesis summary begins with a brief introduction to the engineering context of this research: jet engines and combustors. The next chapter is a comprehensive overview of jet fuels, including composition, liquid properties, chemical kinetics, and modeling. This is followed by a chapter dedicated to the theoretical principles of turbulent combustion, which underpin the simulation methodology and are used in the analysis of the results. The two subsequent chapters describe the simulation methodology and the targeted cases, respectively. The results are then presented in a single chapter, arranged as a logical progression of concepts but not in order of paper number or date of publication. The final chapter summarizes the most important conclusions and provides an outlook for future research.

Chapter 2

Jet engines

Modern mid- to large-scale aircraft rely on air-breathing jet engines for propulsion. The core of a jet engine is a gas turbine with three principal components: a radial compressor, which compresses incoming air and increases its pressure; a combustor, where liquid fuel is injected and ignited; and a turbine, which extracts work from the hot combustion products to drive the compressor. The hot combustion products are expelled as a high-velocity jet behind the engine, producing thrust due to conservation of momentum. If all incoming air passes through these steps, the engine is called a turbojet engine. Modern airplanes more commonly use turbofan engines, which also include a fan mounted in front of the compressor. The fan is driven by the turbine, producing fan thrust (as opposed to jet thrust). Some of the air that passes through the fan continues to the compressor and combustor, while a large fraction passes around the rest of the engine. Fig. 2.1 shows a sketch of a turbofan engine. Helicopters instead use turboshaft engines, in which the turbine work is maximized to power a rotor while the jet thrust is minimized. For the present work, turbojet, turbofan, and turboshaft engines are equivalent: they have similar combustors, operate at largely similar internal pressures and temperatures, and use the same fuels. I will henceforth only use the term "jet engines", even though the research is applicable to turboshaft engines as well.

Jet engine combustors, Fig. 2.1(b), are open systems with few or no moving parts. A number of fuel injectors are placed evenly around the circumference of the engine, feeding a flame enclosed by a set of solid walls referred to as a liner. Modern aircraft typically use annular liners with no solid boundaries separating the fuel injectors. At constant power, air moves through the combustor at a constant rate and the combustion is largely isobaric. Liquid fuel is continuously sprayed directly into the combustor, then vaporized and ignited by the hot combustion products within. The efficiency of this process depends on how easily the fuel is broken up into small droplets, or atomized. The initial transition from a

continuous liquid to a droplet cloud is called primary atomization and can be triggered by a variety of methods. These include pressure atomization, where the fuel is forced through a small high-pressure nozzle; rotary atomization, where the fuel is injected from a moving slinger and atomized by the velocity shear relative to the surrounding gas; and most relevant to this work, airblast atomization, where the fuel is injected as a film along a lip, then atomized by a high-shear airflow at the tip, [9]. Once a droplet cloud has been formed, the droplets continue deforming and separating into smaller droplets in a process called secondary atomization.

Because jet engines invariably use liquid fuel injection, the local Fuel-to-Air Ratio (FAR) where combustion occurs varies from point to point and depends on the rate of mixing between air and fuel. The FAR is typically expressed as the equivalence ratio ϕ, defined as $\phi = \mathrm{FAR}/\mathrm{FAR}_{st}$, where FAR_{st} is the stoichiometric ratio where there is exactly enough air to fully oxidize all the fuel. Some combustion occurs near stoichiometric conditions ($\phi = 1$), resulting in local temperatures of 2000 K or more. Such high temperatures cause the nitrogen in the air to form NO_x, which is harmful to humans and affects the balance of greenhouse gases in the atmosphere, [10]. Some combustion also occurs under fuel-rich conditions ($\phi > 1$), resulting in high emissions of CO, unburnt hydrocarbons, and soot. Combustion at fuel-lean conditions ($\phi < 1$) is comparatively clean. For this reason, stationary gas turbines for electricity generation typically ensure that the fuel is fully vaporized and mixed with air at lean conditions prior to combustion, [11]. However, although clean and efficient, this configuration comes with the risk of flashback, where the flame propagates upward into the fuel system, or blowout, where the flame is unable to remain stable and is extinguished. These risks are unacceptable in aircraft, so the robustness of liquid fuel injection is preferred. A common design method to reduce the NO_x emissions of an engine while guaranteeing stability is to use staged combustion, [12], where an initially fuel-rich flame is impinged by a high-velocity air jet. The air is quickly mixed with the partially burnt fuel, and the combustion process proceeds under lean conditions without a significant amount of activity near stoichiometric conditions.

Jet engine combustors use various flame stabilization mechanisms to maintain a steady flame and prevent blowout, [11]. A common method is to use an aerodynamic design that forms Recirculation Zones (RZ) in the airflow where the velocity reverses, and inject the fuel close to these. The boundary of an RZ has a low mean velocity, allowing a flame to anchor to it. The hot gases from the flame are recirculated toward the fuel, stimulating continuous ignition. RZs easily form in the wakes of bluff bodies and v-gutters but can also form in heavily rotating flows. Many combustors have some air pass through one or several swirlers, i.e., vanes or ducts that induce rotation. If given room, a swirling flow will expand due to centrifugal forces and form a cone of axial flow with a central RZ in the middle; this is called swirl stabilization.

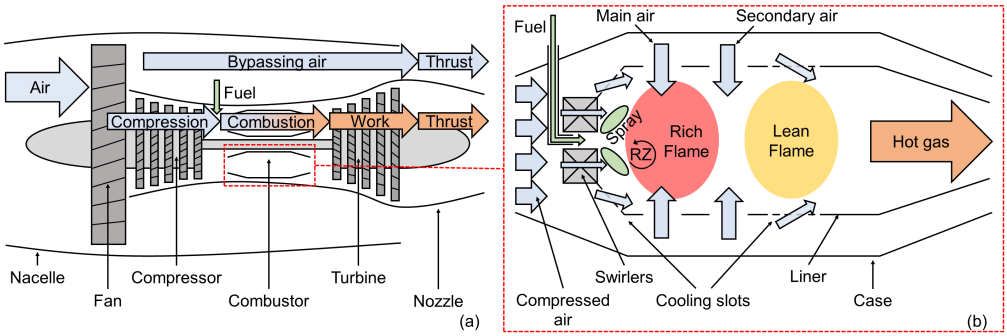

Figure 2.1: Simplified sketch showing the principal components of a turbofan engine (a) and a staged combustor with swirl stabilization (b).

As combustors are essentially confined air ducts, they are prone to forming standing pressure waves. Each combustor has a set of acoustic modes and eigenfrequencies (which may be identified using eigenvalue analysis for a given speed of sound), and these can resonate with other oscillations in the engine that have similar frequencies. The most important of these is the variable heat release rate in the flame, which increases with pressure. Since a sound wave is itself a pressure oscillation, it causes the heat release rate to oscillate at the same frequency as the pressure, which further strengthens the pressure oscillation in a feedback loop. This loop is an example of thermacoustic coupling, and its combined effects are referred to as a thermoacoustic instability, [13]. A sufficiently high amplitude may lead to blowout and damage to the combustor. The strength of the thermoacoustic coupling depends on the time scales associated with the flame and its response to pressure changes. These time scales are influenced by fuel properties, primarily atomizability, volatility, and ignition quality. The ignition quality of jet fuels is quantified by the Cetane Number (CN), which has been demonstrated to affect the range of ϕ in which thermoacoustic oscillations occur, [14].

Conventional jet engines use kerosene fuels, which are distilled from petroleum at temperatures between approximately 200°C and 300°C, [15]. Kerosene is thus less volatile than gasoline but more volatile than diesel. There are many reasons why kerosene is preferred for jet fuels, including its availability and shelf life. The primary operational reasons for using kerosene over heavier hydrocarbon fuels like diesel are its high energy density, low viscosity, and (crucially) its low freezing point, which allows it to remain in liquid form at high altitudes. Conversely, kerosene is also safer than lighter hydrocarbon fuels such as gasoline, thanks to its higher flash point and lower volatility. Kerosene fuels have been standard in aviation for many decades, and in that time, combustors and fuel injectors have been gradually improved and optimized with its properties in mind. The following chapter discusses the properties of jet fuels in greater detail.

Chapter 3

Conventional and alternative jet fuels

This chapter explains the chemical and thermodynamic properties of jet fuels and provides a detailed description of the specific fuels targeted in this work.

3.1 Certification

The most common fuel for civilian aircraft in the US is Jet A, whereas most of the rest of the world uses Jet A-1, which has a slightly lower freezing point, [16]. Jet A is defined by ASTM standard D1655, [17], which includes acceptable bounds for various properties such as viscosity, boiling temperature, and contaminant fraction. The exact properties of the product may vary from batch to batch, but it is still certified Jet A as long as it meets all the requirements. Jet A has historically been a fossil-derived kerosene fuel, and the standards are based on that assumption. For instance, ASTM D1655 specifies a maximum aromatics content but not a minimum content, since a high aromatics content is to be expected when refining petroleum. The standard is thus ill-equipped to cover SAF, which are bio-derived and quite diverse in composition and production method. To solve this issue, an additional standard was introduced: ASTM D7566, [4]. It describes several certified production pathways for neat (i.e., pure, non-fossil) SAF and the requirements for each. Each production pathway also has a certified maximum blending limit with fossil Jet A, which is capped at 50%. If a neat SAF fulfills the requirements, it is blended with fossil Jet A. The resulting fuel blend must adhere to the conventional requirements in ASTM D1655 in addition to the requirements for fuel blends in ASTM D7566 (although D7566-compliant fuels are treated as D1655-compliant without duplicate testing). These additional requirements include, for example, a minimum aromatics content of 8% by volume. In other words, fossil-SAF blends have more stringent requirements than conventional fossil fuels.

3.2 Composition and basic characteristics

Conventional jet fuels consist of a diverse range of hydrocarbons of different types and sizes, with carbon numbers typically ranging from 7 to 16 and peaking at 11 to 12, [18]. These hydrocarbons already exist in petroleum and are simply extracted by distillation. Alternative jet fuels, on the other hand, are chemically synthesized from ingredients that are very different from the final product, from small alcohols like ethanol and butanol to large polymers like lignin. They thus consist of a narrower range of hydrocarbons with average sizes potentially quite different from those found in conventional fuels.

Setting minor species and pollutants aside, the components of jet fuels may be divided into four categories of hydrocarbons: straight n-paraffins, branched iso-paraffins, cyclical saturated cyclo-paraffins, and cyclical unsaturated aromatics, [18]. Figure 3.1 shows a seven-carbon example from each category. N- and iso-paraffins have the highest H/C ratios, i.e., the highest numbers of hydrogen atoms per carbon atom. The ratio decreases with size, and the mean H/C is around 2.2 for jet fuels. Because C —— H bonds are relatively energetic, H/C is correlated with heat of combustion. In this context, cyclo-paraffins are all saturated hydrocarbons containing closed rings; most cyclo-paraffins in conventional fuel have one or two rings, [18], but Ruan *et al.*., [19], detected substantial amounts of three-ring and four-ring cyclo-paraffins in a lignin-based SAF. Aromatics contain benzene rings, which are unsaturated and have relatively low H/C. The aromatics in conventional jet fuel typically contain one or two rings, [18]. The high carbon content and stability of benzene rings make aromatics less likely to undergo complete combustion and more likely to form carbon-rich intermediate species such as C_2H_2 and C_2H_4. These can then coalesce into larger multi-ring aromatics called Polycyclic Aromatic Hydrocarbons (PAH), which form the nuclei of soot particles. Note that cyclo-aromatics, which contain both saturated and unsaturated carbon rings, may be present in jet fuel in small amounts but are not discussed here, [18].

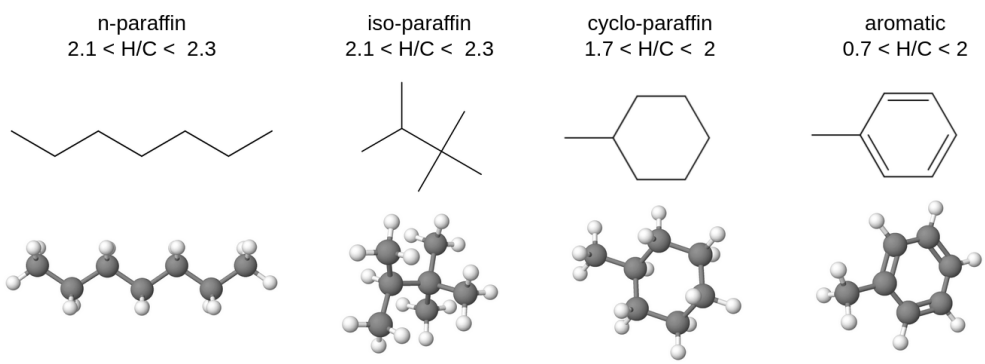

Figure 3.1: The four main categories of jet fuel components. The shown species all have seven carbon atoms and are, from left to right: n-heptane, 2,2,3-trimethylbutane, methylcyclohexane, methylbenzene. The H/C ratios are approximate and depend on structure and carbon number.

Figure 3.2 shows six important fundamental properties for each component class: CN, heat of combustion, boiling temperature (T_{boil}), dynamic viscosity (μ), density (ρ), and surface tension (σ). All temperature-dependent properties are given at 298.15 K. CN is approximately inversely correlated with the time required for the fuel to auto-ignite when exposed to a high temperature. The heat of combustion is given as the Higher Heating Value (HHV), which corresponds to the energy released per kilogram of fuel during combustion in addition to the energy extracted by cooling the products back to 298.15 K. Only carbon numbers between 6 and 9 are shown, as data is less prevalent for larger species (except for n-paraffins) and not all are liquids in pure form at room temperature. Furthermore, all components except n-paraffins have many possible permutations, making it difficult to find a set of representative species.[1]

Because each iso-paraffin has not been widely studied, their viscosity is highly uncertain; therefore, the viscosity given in Fig. 3.2 is not measured but instead computed using the Joback method, [20]. The chosen cyclo-paraffins all contain a single six-carbon ring; the first one is purely cyclical, whereas the others also contain a single straight chain. The first aromatic is benzene (the only six-carbon aromatic), whereas the larger aromatics contain a single benzene ring with additional methyl groups. Since there are many other possible options and only a limited range of carbon numbers are considered, the trends in Fig. 3.2 are not all universal principles but may be used as rules of thumb for explaining the different properties of fuels with distinct compositions. The following trends may be considered significant:

- CN is highest for n-paraffins and much lower for iso-paraffins. It is very low for aromatics.
- The energy content (HHV) is largely determined by the H/C ratio. N-paraffins and iso-paraffins thus have the highest (and approximately equal) HHV. Cyclo-paraffins have slightly less energy and aromatics much less.
- T_{boil} is strongly correlated with carbon number, and iso-paraffins have relatively low T_{boil}.
- Viscosity tends to increase with carbon number. (Although the purely cyclical cyclohexane and benzene have relatively high viscosities.)
- Aromatics have the highest density, followed by cyclo-paraffins, then n- and iso-paraffins with approximately equal density.

[1]The species used here are: 2,2-dimethylbutane, 2,2,3-trimethylbutane, 2,2,4-trimethylpentane, 2,2,5-trimethylhexane, cyclohexane, methylcyclohexane, ethylcyclohexane, propylcyclohexane, benzene, methylbenzene, 1,4-dimethylbenzene, and 1,2,4-trimethylbenzene.

- Aromatics have the highest surface tension, followed by cyclo-paraffins, then n-paraffins, then iso-paraffins. Surface tension increases with carbon number for n-paraffins.

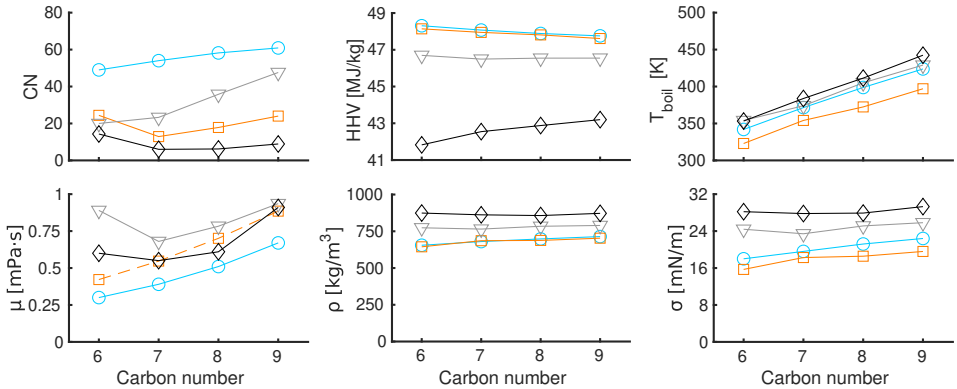

Figure 3.2: CN, HHV, T_{boil}, μ, ρ, and σ as functions of carbon number. Legend: n-paraffins (cyan), iso-paraffins (orange), cyclo-paraffins (gray), aromatics (black), measured property (solid line), estimated property (dashed line). Sources for measured properties: [21, 22, 23, 24].

3.3 Reference fuels

Scientific studies on alternative jet fuels typically focus on the set of well-defined reference fuels proposed by the US-based National Jet Fuels Combustion Program, [25]. These are divided into three categories: A, B, and C. Category A contains three fuels which represent typical batches of Jet A as well as the military jet fuels JP-8 and JP-5. Category B features fuels with unacceptable properties and is not relevant for this work. Category C contains "extreme" fuels with properties close to or outside the allowances in ASTM D1655 and D7566. One category C fuel, C1, is a neat SAF produced via the ATJ pathway. C5 is a synthetic fuel with a low, flat distillation curve and very high aromatics content. This work targets Jet A, C1, and C5, with JP-5 included as an additional point of comparison in some parts. Jet A represents conventional fossil jet fuel, and C1 represents neat SAF. Although neat SAF can vary widely in composition, as already explained, C1 is somewhat representative with its very high iso-paraffin content and low aromatics content, both of which are typical of most SAF. C5 does not represent any real jet fuel but is an excellent complement to Jet A and C1 with its high aromatics content and volatility. Jet A, C1, and C5 thus represent a very wide range of thermodynamic and chemical properties.

The top row of Fig. 3.3(a) shows measured composition spectra for Jet A, C1, and C5, consisting of the mass fraction of the four component classes across different carbon numbers,

[18]. Jet A, a fossil fuel, contains a wide range of components of many different sizes. C1 is very different, consisting of virtually 100% iso-paraffins, of which only two (iso-dodecane and iso-hexadecane) dominate the spectrum. C5 is a mix of trimethylbenzene, n-decane, iso-decane, and iso-undecane. If the combustion of these fuels is to be simulated in an informative and reproducible way, they must first be reduced to a specific blend of representative components, i.e., a surrogate. This is a major simplification for Jet A, but not for C1 and C5, which already consist of only a few components. The surrogates presented in the bottom row of Fig. 3.3(a) were proposed by Rui *et al.*, [26], and are the basis for the chemical reaction mechanisms used in this work. Jet A is reduced to a single species per component class. The C1 surrogate is identical to the real fuel, except that trace iso-paraffins are neglected. The C5 surrogate is a very slight simplification as it replaces the minor iso-undecane contribution with iso-decane. The measured distillation curves of the real fuels are given in Fig. 3.3(b), and show the cumulative distillation progress across a range of temperatures. Jet A has a mostly linear curve due to its wide and smooth composition. C1 has a non-linear curve as it mostly consists of only two components, and its average T_{boil} is lower than that of Jet A. C5 has the lowest curve, which is also very flat as all of its components boil at the same temperature.

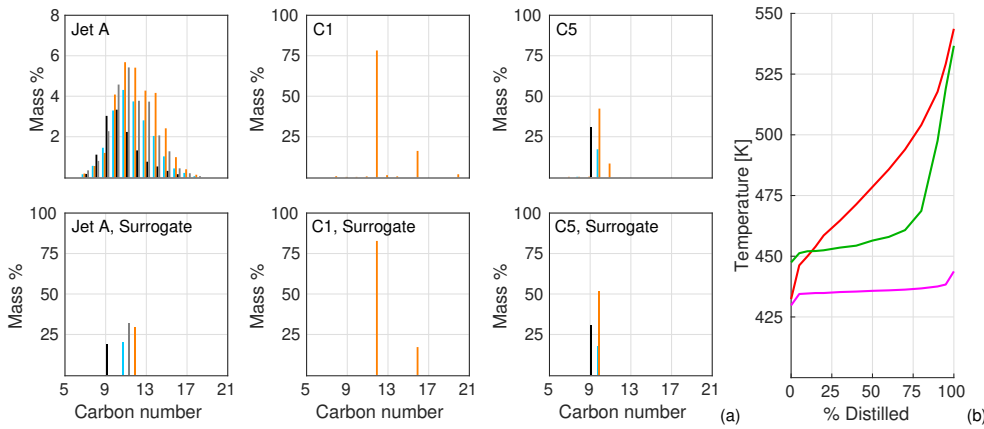

Figure 3.3: Measured (top) and surrogate (bottom) composition spectra (a) alongside distillation curves for all fuels (b). Measured spectra are obtained from Edwards, [18], and surrogate spectra from Xu *et al.*, [26]. Note the trace amounts of iso- and n-paraffins in the measured spectra of C1 and C5. Legend (a): n-paraffins (cyan), iso-paraffins (orange), cyclo-paraffins (gray), aromatics (black). Legend (b): Jet A (red), C1 (green), C5 (magenta).

The basic properties of Jet A, C1, and C5 are summarized in Table 3.1. The Lower Heating Value (LHV), which excludes the energy extracted by cooling the products, is used to quantify the heat of combustion. The component fractions refer specifically to the surrogate compositions but are also fairly accurate for the real fuels. The Molecular Weight (MW) is determined by the average size of the components, with C1 being the largest and C5 the smallest. LHV is determined by composition; C1 only has high-energy iso-paraffins and

thus the highest LHV. Although C5 has the highest concentration of low-energy aromatics, its LHV is only slightly lower than that of Jet A due to the latter fuel's abundance of mid-energy cyclo-paraffins. Based on the surrogate H/C, the "average" species would be $C_{11.4}H_{21.7}$, $C_{12.5}H_{27.1}$, and $C_{9.7}H_{18.7}$ for Jet A, C1, and C5, respectively. This presents a problem for chemical reaction mechanisms that model the fuel as a single species, as non-integer carbon and hydrogen numbers are typically not supported in combustion codes. To solve this, the formulas are rounded to $C_{11}H_{22}$, $C_{13}H_{28}$, and $C_{10}H_{19}$. This rounding comes with the disadvantage of changing the H/C ratio trend among the fuels: the measured H/C of Jet A, C1, and C5 are 1.91, 2.16, and 1.93, whereas their modeled H/C are 2.0, 2.15, and 1.9. The discrepancy is largest for Jet A, and hydrogen-heavy species (e.g., water vapor) are consequently over-represented in the emission predictions for Jet A.

Table 3.1: Summary of thermochemical properties of the targeted jet fuels, obtained from [18]. Surrogate compositions and LHV are obtained from [26].

	Jet A	C1	C5
n-paraffins [mol %]	19.33	0	16.72
iso-paraffins [mol %]	26.09	100	48.90
cyclo-paraffins [mol %]	31.16	0	0
aromatics [mol %]	23.42	0	34.38
MW [g/mol]	159	178	135
LHV [MJ/kg]	43.1	43.9	43.0
CN [-]	48.3	17.1	39.6
Surrogate formula	$C_{11.4}H_{21.7}$	$C_{12.5}H_{27.1}$	$C_{9.7}H_{18.7}$
Modeled formula	$C_{11}H_{22}$	$C_{13}H_{28}$	$C_{10}H_{19}$
Actual H/C (by mol)	1.91	2.16	1.93
Modeled H/C (by mol)	2.0	2.15	1.9

3.4 Liquid properties

As the fuel droplets propagate through the combustor, they are heated by the surrounding air and the flame until they become either saturated or supercritical. The critical temperature of Jet A is approximately 700 K, [27]. To simulate this, one must incorporate a model that provides all relevant properties (e.g., μ, σ) for any temperature between the injection temperature (which could be 300 K or lower) and the saturation temperature. Such a model was developed for Jet A, JP-5, C1, and C5 as a part of this work. It consists of correlations for c_p (specific heat capacity), μ, p_v (vapor pressure), ρ, σ, and ΔH_{vap} (heat of vaporization) as functions of temperature. The effect of pressure is neglected by assuming that the liquid is incompressible. The correlations are shown in Fig. 3.4 alongside available physical measurements, [18]. These measurements were used to fit the model,

but several approximations had to be made to extrapolate to higher temperatures. Additional data points could, for example, be obtained from a mass-weighted average of the pure substances included in each fuel surrogate. The largest uncertainty in the model lies in p_v, which increases exponentially with temperature but is largely unknown between the normal boiling point T_{boil} (squares) and the critical temperature T_{cr} (crosses). The heat of vaporization is given as $h_v - h_l$, where h_v and h_l are the vapor and liquid enthalpies; this notation is used to highlight that the heat of vaporization is exactly equal to the difference between the vapor enthalpy defined in the HyChem model, [26], and the liquid enthalpy obtained by integrating the liquid heat capacity. For more details about the development and limitations of the liquid model, see paper IV.

The trends in Fig. 3.4 can be explained by considering the composition of each fuel. The composition of JP-5 is quite similar to that of Jet A but has more cyclo-paraffins and aromatics, which increase ρ, μ, and σ. Its average MW is also slightly higher, decreasing p_v. C1, which is assumed to consist of 100% iso-paraffins, has the lowest ρ and σ; were it not for its relatively high average MW, it would also have the lowest μ and p_v. C5 contains a large fraction of high-ρ, high-σ aromatics, but its low average MW and complete lack of cyclo-paraffins result in ρ and σ similar to C1. Its low MW significantly increases p_v and reduces μ, however, making C5 the most volatile fuel as well as the most easily atomized.

3.5 Gas-phase kinetics

Once vaporized, the fuel starts to ignite. The process begins with thermal decomposition, where heat causes the fuel components to break apart and form smaller hydrocarbons (carbon number <5). This process was described in detail by Wang *et al.*, [28]. Some hydrogen is abstracted and forms free hydrogen (H) or H_2, leaving unsaturated hydrocarbons such as ethylene (C_2H_4) and propylene (C_3H_6). The joints of heavily branched iso-paraffins are partly preserved as iso-butene (i-C_4H_8). The benzene rings in aromatics are separated from their side branches. According to Xu *et al.*, [26], it is the distribution of a relatively small number of these decomposition products that largely determines the subsequent oxidation behavior of the fuel. In particular, they identified C_2H_4, H_2, CH_4, C_3H_6, 1-C_4H_8, i-C_4H_8, benzene (C_6H_6), and toluene (C_7H_8) as important species to capture when modeling the decomposition process.

Thermal decomposition is followed by oxidation, where the decomposition products react with oxygen from the air and release heat. Different decomposition products are oxidized at different rates; for example, the relatively stable i-C_4H_8 ignites more slowly than C_2H_4, contributing to the low CN of C1. One way to quantify reactivity is the laminar flame speed s_u, which is defined as the propagation speed of the flame front into the unburnt reactants in unstrained laminar flow, i.e., how quickly combustion spreads through the

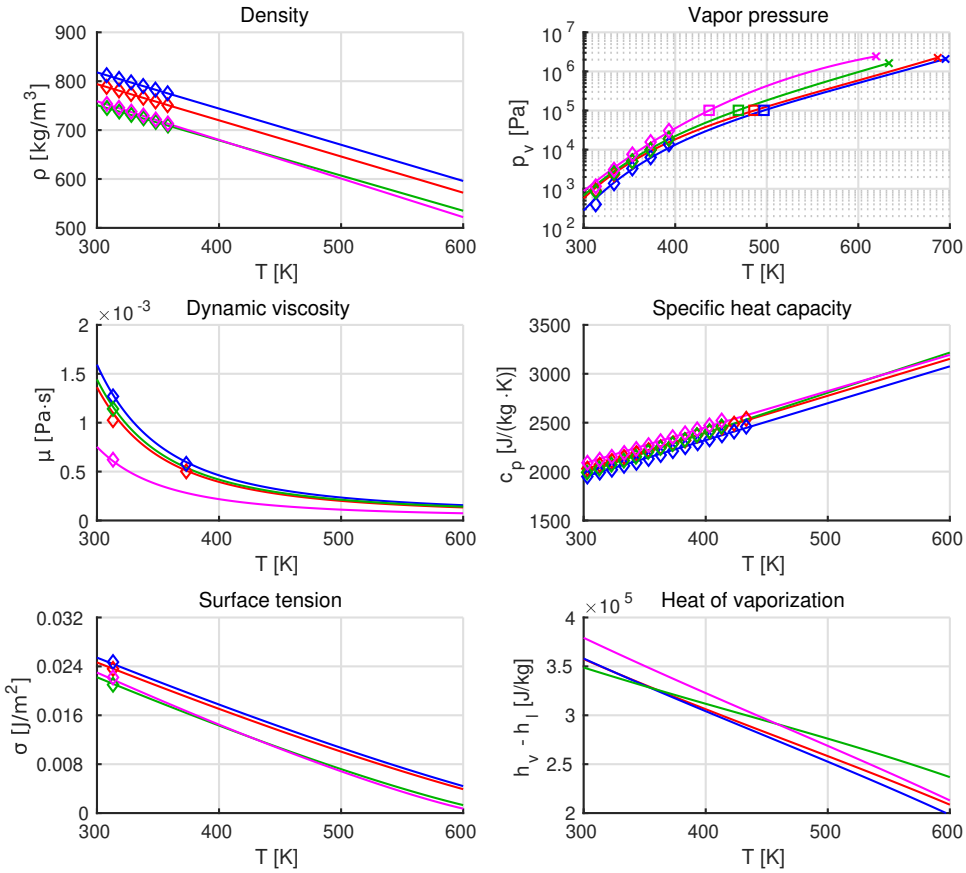

Figure 3.4: Derived model correlations for ρ, p_v, μ, c_p, σ, and ΔH_{vap} (shown as h_v - h_l). Legend: Jet A (red), JP-5 (blue), C1 (green), C5 (magenta), experimental measurements, [18], (diamonds), average normal boiling points (squares), estimated critical points (crosses).

reactants. Table 3.2 shows s_u predictions for the most important decomposition products, as predicted by the detailed Creck 17790 reaction mechanism, [29], in Ansys Chemkin-Pro, [30]. Predictions for (surrogates of) Jet A, C1, and C5 are included for comparison. The fuel mixtures naturally have relatively low s_u, as their combustion path also includes the thermal decomposition step. The alkenes (C_2H_4, C_3H_6, 1-C_4H_8), which are commonly produced by the decomposition of straight carbon chains, are quite reactive and have high s_u. C_2H_4 burns the fastest and is also the most prevalent of the alkenes, [26]. The flame speed is considerably lower for i-C_4H_8, which is produced in abundance during the thermal decomposition of iso-paraffins; this is explained by the resonant stability of iso-butenyl (i-C_4H_7), an intermediate species in the oxidation pathway of i-C_4H_8. Benzene rings also burn relatively slowly due to their low H/C ratio, [31].

Jet fuel combustion is extremely complex chemically, involving thousands of intermediate

Table 3.2: Stoichiometric s_u of important thermal breakdown products, as predicted by the detailed Creck 17790 reaction mechanism, [29], at 403 K. Predictions for surrogate Jet A, C1, and C5 mixtures are included for comparison.

Species	s_u [cm/s]
C_2H_4	105.8
C_3H_6	70.7
1-C_4H_8	72.2
i-C_4H_8	60.9
CH_4	60.8
Benzene	65.0
Toluene	54.6
Jet A (surrogate)	57.6
C1 (surrogate)	57.3
C5 (surrogate)	55.2

species and tens of thousands of reactions. It can be modeled directly using detailed reaction mechanisms, e.g., Creck 17790, that directly compute the rates of most elementary reactions involved. (Although even detailed mechanisms include simplifications, such as lumping all isomers of i-$C_{12}H_{26}$ together in a single species.) These mechanisms may be used in 0D or 1D simulations but are far too computationally expensive for anything but the smallest CFD simulations. LES in 3D requires heavily reduced and optimized reaction mechanisms to keep the computational cost on a realistic level. Historically, these have been global mechanisms with 1–4 reactions, e.g., [32], that convert the fuel into CO_2 and H_2O directly, sometimes with CO as an intermediate. Although computationally efficient, mechanisms with that level of reduction are not suitable for differentiating between the combustion characteristics of different fuels because they a) do not adequately capture fundamental properties like s_u and b) do not include any of the crucial thermal decomposition products that determine the kinetics of each fuel. A *skeletal* or *pathway-centric* mechanism addresses these issues by including as many species and reactions as required to capture the most crucial reaction pathways, while less important reactions are ignored or lumped into other reactions. With up to several hundred reactions, these mechanisms are much more demanding than global alternatives but still feasible to use in LES with high-performance computing.

At the time of writing, there are two major families of skeletal reaction mechanisms[2] available for Jet A, JP-5, C1, and C5: HyChem, [28, 26, 33], and Zettervall, [34, 35]. Both model the fuel as a single representative species that undergoes a short series of heavily simplified and lumped decomposition steps. Each fuel decomposes into a specific distribution of decomposition products, which are oxidized in a semi-detailed series of reactions.

[2]These mechanisms are considered skeletal by CFD standards, but a chemist might not consider them detailed enough for that designation.

Most elementary reactions involving the smallest species (H_2–O_2 and C_1–O_2 chemistry) are accounted for.

The HyChem family includes several mechanism versions with varying degrees of complexity; the ones used here are the "skeletal" versions with ∼50 species and ∼250 reactions. The Jet A and JP-5 mechanisms include additional species and reactions specifically intended to capture the Negative Temperature Coefficient (NTC) effect, where the fuel auto-ignites relatively quickly at low temperatures. The C1 and C5 mechanisms do not have this feature and should not be used in simulations where low-temperature ignition behavior is key.

The Zettervall mechanisms constitute a large family of highly reduced mechanisms with ∼30 species and ∼80 reactions. At high temperatures, the fuel undergoes a single thermal decomposition step, producing C_2H_4, C_2H_5, C_2H_3, CH_2, and CH. At lower temperatures, the fuel instead undergoes a series of lumped oxidation steps that terminate in a ketone and OH radical. The rates of these low-temperature reactions determine the ignition time, and all Zettervall mechanisms are capable of capturing the NTC effect. The decomposition products react in a reduced sub-mechanism, the products of which are finally oxidized in relatively detailed C_1–O_2, H_2–O_2, and CO–O_2 base mechanisms. The Zettervall mechanisms are more computationally efficient than HyChem, requiring ∼70% less computational time. The downside is that they include fewer intermediate species, particularly thermal decomposition products like i-C_4H_8 and benzene, the impact of which may not be accurately captured. Another potential downside is that the base chemistry, particularly reactions involving the hydrogen radical H, are calibrated for each fuel to achieve accurate predictions of fundamental flame properties. The most recent Zettervall mechanisms for jet fuels are the Z79 mechanisms, so called because they contain 79 reactions. These are presented in paper II, co-authored by Dr. Zettervall.

The remainder of this chapter is dedicated to evaluating and comparing the HyChem, Z79, and Creck 17790 mechanisms. Fig. 3.5 contains predictions of the laminar flame speed s_u, the ignition delay time τ_{ign}, and the extinction strain rate K_{ext} computed in Ansys Chemkin-Pro, [30]. Experimental data are included for comparison, color-coded based on fuel. To compute s_u, an unstrained laminar flame is simulated in 1D at atmospheric conditions with an unburnt temperature of 403 K. Simulations are carried out across a range of ϕ, as shown in the figure. To compute τ_{ign}, a stoichiometric mixture at 10 bar is allowed to auto-ignite isochorically, with τ_{ign} defined as the time required for ignition to occur. Simulations are carried out in 0D for a range of initial temperatures T, which are conventionally expressed as $1000/T$. To compute K_{ext}, a 1D counterflow flame is simulated at atmospheric conditions. The flame is stabilized between two opposite-facing jets with a separation of 7 mm. One jet consists of a fuel-air mixture at 393 K and $\phi = 0.85$, with the other consisting of pure nitrogen at 300 K. A series of steady simulations are carried out, each iteratively altering the velocity of the jets to slightly change the maximum flame temperature T_{max} and maximum velocity strain rate K_{max}. The maximum possible K_{max}

identified by this process is equivalent to K_{ext} and corresponds to the strain rate at which flame extinction occurs.

For s_u, all mechanisms reproduce experimental measurements quite well. The uncertainty associated with such measurements is quite high and may vary based on fuel batch and measurement technique; this is exemplified by the difference between the Jet A measurements from Xu *et al.*, [26], and Kumar *et al.*, [36], which both correspond to Jet A. The difference between the fuels in terms of s_u should therefore be considered insignificant. A more important question, from a modeling perspective, is how each mechanism family predicts the fuel trend. At lean to stoichiometric conditions, both HyChem and Z79 predict similar s_u for Jet A and C5 but lower s_u for the iso-paraffinic C1. At fuel-rich conditions, Z79 predicts that C5 drops off more sharply than Jet A. Creck 17790 predicts virtually identical s_u for all fuels, especially Jet A and C1. It is reasonable to expect a lower laminar flame speed for C1 since it produces high amounts of slow-reacting i-C_4H_8, and heavier species are less diffusive than lighter species, [37].

For τ_{ign}, the HyChem mechanisms for C1 and C5 stand out at low temperatures as they lack NTC modeling. There is no experimental data to verify the potency of the NTC effect for these fuels, but it is reasonable to assume that it is somewhat similar to kerosene. C5 ignites more slowly than Jet A on the whole due to its high concentration of low-CN, slow-burning aromatics. The low CN of C1 is visible at high temperatures, where the low reactivity of i-C_4H_8 becomes rate-limiting. However, at intermediate temperatures ($\sim$1000 K), C1 ignites more quickly than Jet A due to the relatively rapid thermal breakdown of iso-paraffins. The same trends are predicted by the Z79 mechanisms, in addition to an estimated NTC effect based on τ_{ign} for compounds with similar CN. The detailed Creck 17790 mechanism reproduces the experimental measurements for C1 and C5 quite well but overpredicts τ_{ign} for Jet A. The error likely stems from the relative simplicity of the Jet A surrogate, demonstrating that the accuracy of a detailed mechanism is limited by the surrogate definition.

All mechanisms agree that C1 has the lowest K_{ext}. This is expected considering its documented sensitivity to lean blowout, [38]. The HyChem and Z79 mechanisms predict similar K_{ext} for C1, whereas Creck 17790 predicts a considerably higher value. Creck 17790 appears to systematically predict a higher reactivity for C1 compared to the other mechanisms, as evidenced by its high s_u, low τ_{ign}, and high K_{ext}. All mechanisms are in relatively close agreement concerning the K_{ext} of Jet A but differ greatly in their predictions for C5. This is likely due to the prevalence of benzene rings in the flame, which add complexity to the extinction problem. Finally, the Z79 mechanisms predict relatively low T_{max} compared to the other mechanisms, which is also true in the laminar simulations.

Which mechanism family is preferable for LES of alternative jet fuel combustion: HyChem or Z79? In cases where low-temperature ignition is key or computational cost is a critical

limiting factor, Z79 should be used. Otherwise, both mechanism families are well-validated for s_u and τ_{ign}, and predict the same fuel trend for K_{ext}. HyChem is older and has been used more widely in the literature, making comparisons with previous studies easier; for this reason, HyChem is used in papers I, IV, and V. Paper III predates Z79, but contains a comparison between HyChem and Z77, a precursor mechanism for JP-5. Paper II is dedicated to comparing the HyChem and Z79 mechanisms in LES.

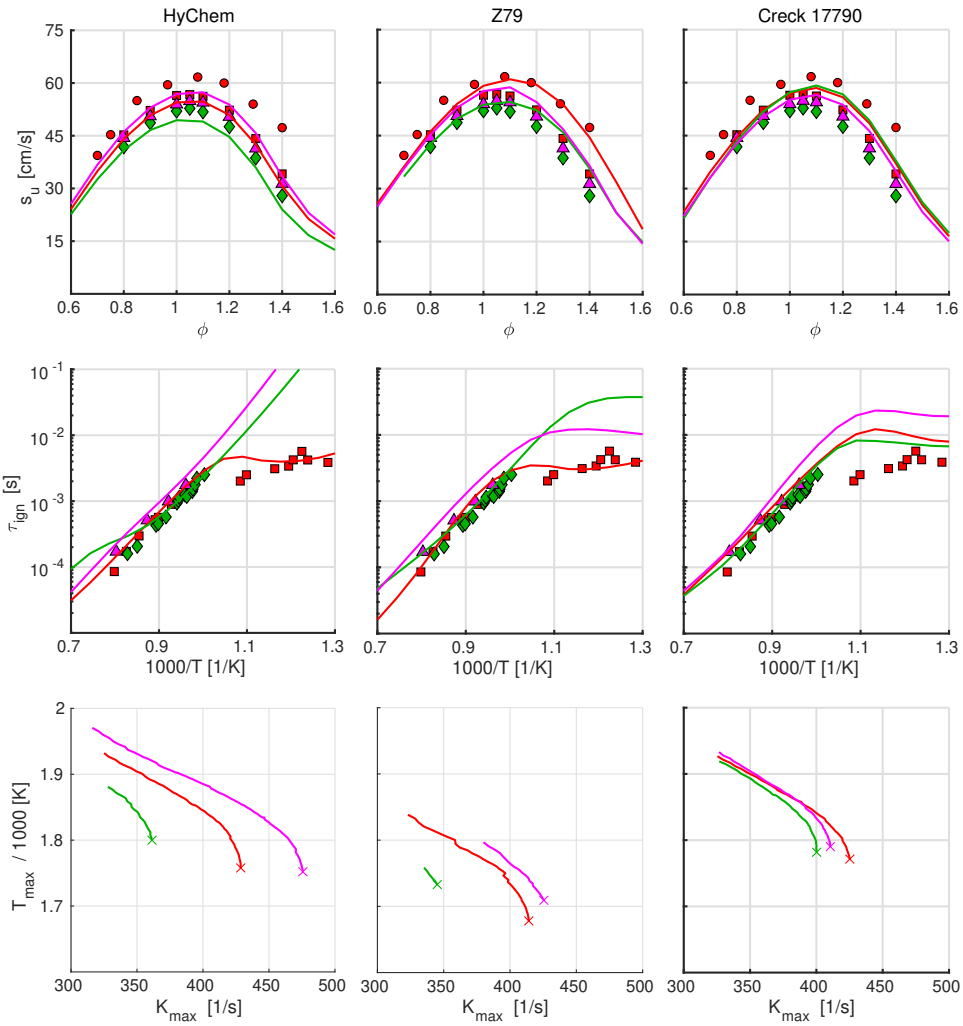

Figure 3.5: Predicted fundamental combustion properties. Top to bottom: s_u, τ_{ign}, K_{ext}. Left to right: HyChem, Z79, Creck 17790. Legend: Jet A (red), C1 (green), C5 (magenta), experimental measurements, [26, 33], (squares for Jet A, diamonds for C1, triangles for C5), additional Jet A measurements, [36], (circles).

Chapter 4

Turbulent combustion and its modeling

This chapter provides a brief overview of the theoretical principles underpinning turbulent combustion and its modeling.

4.1 Turbulent flow

The gas flow through a jet engine is heavily turbulent, which means that it follows a chaotic and unsteady pattern characterized by the constant formation, deformation, and dissipation of eddies (i.e., localized high-vorticity regions). Mathematically, this complex behavior results from the non-linearity of the Navier-Stokes equations, which govern the motion of fluids, [39]. Turbulent flows are diffusive; a substance (whether gaseous, liquid, or particulate) injected into a turbulent airflow will be mixed with the surrounding air and spread out. This is important for combustors, where the fuel must be efficiently mixed into the airflow to ensure rapid vaporization and a stable flame. Turbulence is best understood as a multi-scale process where kinetic energy is transferred between different scales of time and length via an energy cascade. As air moves through the system, the kinetic energy of the bulk flow is transferred to large eddies; these form in regions of high velocity shear, such as the edges of RZs, where the flow is subjected to bending and rotation. The large eddies experience more velocity shear between themselves and the environment, causing them to stretch and break up into smaller eddies. Due to conservation of momentum, angular momentum, and energy, the smaller eddies retain the kinetic energy of the large eddies but occupy smaller scales of time and length. The cascade process continues down to the smallest possible turbulent scales, the Kolmogorov scales, where the convective forces associated

with the eddies are small enough to be dampened by viscous forces. The eddies dissipate, and their kinetic energy is converted to heat.

4.2 Premixed, non-premixed, and partially premixed flames

A flame is essentially a flow in which combustion reactions occur, and like any flow, it can be laminar or turbulent. Flames are further classified as either premixed, non-premixed, or partially premixed, depending on whether the fuel is mixed with the oxidizer before combustion, [40]. Spray flames may be classified as partially premixed flames.

In premixed flames, the fuel is homogeneously mixed with the oxidizer before it combusts. The FAR is well-defined, and the temperature and emission profile of the flame are relatively easy to predict based on LHV and H/C. The flame is characterized by a sheet of high chemical activity, a flame front, between the cold reactants and the hot combustion products. Most of the heat release happens in a thin layer in the middle of this sheet, the inner reaction zone, where small hydrocarbons are oxidized in exothermic reactions that also produce energetic combustion radicals. On the burnt side, the radicals are gradually consumed in further exothermic reactions until chemical equilibrium is reached; the relatively broad region where this occurs is called the postflame zone. On the unburnt side, heat and radicals from the inner reaction zone are diffused into the reactants, triggering the thermal decomposition of the fuel; the region where this occurs is called the preheat layer.

In purely non-premixed flames, the fuel and oxidizer are initially separate and immediately react when they come into contact. Combustion occurs near stoichiometric conditions, resulting in a very high temperature and NO_x formation. A postflame zone forms downstream of the inner reaction zone, and the preheat layer extends into both the fuel and oxidizer streams. The main benefits of non-premixed flames are that they do not require any bulky premixing apparatus and that they cannot experience flashback since the fuel and oxidizer streams are not separately combustible. Whereas ϕ is generally preferred for quantifying the FAR in premixed flames, the mixture fraction z is more useful for non-premixed flames. The mixture fraction is defined as the local mass fraction of matter originating from the fuel; if the air is assumed to consist of only oxygen and nitrogen, and the fuel only of hydrocarbons, then the mixture fraction is equivalent to the local mass fraction of hydrogen and carbon atoms (regardless of which species they are part of). The mixture fraction is conserved during combustion.

In partially premixed flames, such as spray flames, fuel is injected into the oxidizer and partially mixed with it before combustion. Flashback can occur, but can at most propagate to the fuel injector. The local z varies from point to point, but if there is significant premixing, most of the combustion occurs near the global ϕ set by the overall FAR in the system. In

the case of limited premixing, combustion occurs across a wide range of z with a significant amount near stoichiometry. Large flames may consist of relatively non-premixed segments near the fuel injector and relatively premixed segments further downstream.

Although spray flames may be categorized as partially premixed flames, they also involve a phase transition from liquid to vapor. The vaporization rate, which is accelerated by efficient mixing with the airflow, affects where the flame can stabilize; the flame front may not release enough energy for reactions to propagate upstream if some of that energy is used for the phase transition instead of increasing the fuel temperature. The atomization and breakup of the liquid fuel also affect the behavior of a spray flame, as described by Chiu *et al.*, [41]. If the spray consists of many small droplets, these typically form a fuel-rich spray core separated from the flame front by a layer of vaporized fuel. If there are fewer, larger droplets, the flame can penetrate the spray and fill the spaces between relatively dense clusters of droplets in a process called group combustion. In dilute sprays, the droplet separation may be large enough that each is individually surrounded by a non-premixed flame; this is referred to as single droplet combustion.

4.3 Turbulence-chemistry interaction

Flames are heavily affected by turbulence. Eddies wrinkle and deform the flame front while the preheat layer and postflame zone are broadened by turbulent diffusion. On a microscopic level, chemical reactions are localized in intermittent turbulent fine structures, [42]. Combustion also affects turbulence in return, as the heat it releases causes volumetric expansion that reduces vorticity, [43]. Premixed flames are typically analyzed using the non-dimensional Karlovitz number, defined as $\mathrm{Ka_T} = \tau_c/\tau_K$, and Damköhler number, defined as $\mathrm{Da_T} = \tau_I/\tau_c$, where τ_c is the time scale of chemical reactions, τ_K the Kolmogorov time scale, and τ_I the integral (largest) length scale of turbulence, [40]. Theoretically, if $\mathrm{Ka_T} < 1$, the combustion reactions occur faster than even the fastest turbulent motions, which means that the flame front is largely undisturbed by turbulence. Such a flame has a laminar-like structure and is referred to as a flamelet. The flamelet is still suspended in a turbulent flow that wrinkles and deforms it, but it maintains its thin, laminar-like structure. If $\mathrm{Ka_T} > 1$, turbulent motions are rapid enough to enter the preheat layer and broaden it, increasing diffusion into the reactants. This is called the "broadened preheat, thin reactions" or simply "thin reactions" regime and is typical for premixed flames in practical applications. The terminology refers to the notion that the time scales of the inner reaction zone are still too short for it to be disturbed by turbulence, allowing the inner reaction zone to maintain a thin sheet-like shape with reactants on one side and products on the other. If $\mathrm{Ka_T}$ becomes sufficiently high, the inner reaction zone is also broadened by eddies, and the flame enters the "broadened reactions" or "distributed reactions" regime, [44].

Fully non-premixed flames are driven by diffusion between reactants and products, which is enhanced by turbulence. (Non-premixed flames are also called "diffusion flames".) The analysis is often based on the scalar dissipation rate, which is proportional to $|\nabla z|^2$ and thus high in regions with high strain rate, [40]. A high scalar dissipation rate corresponds to strong turbulent diffusion of both heat and species, but if it becomes too high, the heat released from the combustion reactions is too low to balance the heat transported away from the inner reaction zone and the flame is quenched. The strain rate required to trigger this is the extinction strain rate, K_{ext}, discussed in the previous chapter.

Partially premixed flames interact with turbulence as both premixed and non-premixed flames do, but the presence of both modes leads to some emergent phenomena. The local mode of combustion can be identified using the Takeno flame index, [45], which is based on the gradients of fuel and oxidizer; parallel gradients imply premixed combustion, whereas antiparallel gradients imply non-premixed combustion. In a partially premixed flame where combustion occurs at both lean and rich conditions, a "triple flame" structure can emerge, [40]. A triple flame partly consists of a curved premixed flame front with variable z. The inflection point of the flame front coincides with the stoichiometric z, as it provides the maximum flame speed. Behind the inflection point, a non-premixed flame front perpendicular to the premixed one extends into the burnt region, where surplus hydrocarbons and carbon-heavy species like CO are diffused from the rich side and meet surplus oxygen from the lean side. The propagation of the triple flame into the reactants can thus be understood in a premixed context (e.g., with $\mathrm{Ka_T}$), whereas the size of the postflame zone and its formation rates of various emissions can be understood in a non-premixed context (e.g., with scalar dissipation rates). Turbulence enhances the premixing between fuel and oxidizer. This is especially true for sprays, where turbulence helps disperse and break up droplets. However, since flame propagation is governed by the premixed mode, and turbulence increases the flame propagation rate by enhancing the diffusion of heat and radicals into the unburnt mixture, a high turbulent intensity can result in the flame moving closer to the fuel injector where the mixture is less well-mixed.

4.4 CFD and LES

A typical CFD simulation involves defining a set of governing equations for the flow, usually derived from the Navier-Stokes equations with some terms added or removed to suit the problem at hand. The governing equations are transport equations for conserved quantities; these always include equations for mass and momentum, but an equation for energy is also required unless the flow is isothermal. If the chemical composition of the fluid can change, transport equations for the mass fractions of all involved chemical species are also required (although they are sometimes reduced to a single abstract scalar such as the flame progress variable). The governing equations are unclosed and thus require additional equations,

based on assumptions about the problem, for closure. These include the assumption of a Newtonian fluid, transport mechanisms such as Fourier heat conduction, and equations of state such as the ideal gas law.

When an appropriate and closed set of equations has been decided on, they are solved numerically. A spatial domain is designed for the problem, consisting of a 2D or 3D model of the fluid-containing volume with boundaries placed where appropriate boundary conditions may be imposed. The domain is then split into a discrete number of cells, or subvolumes, which together form a mesh. The continuous governing equations are solved using this mesh by assuming linearity between neighboring cells. In other words, each transport equation is discretized into a finite linear equation system with dimensions determined by the number of cells in the mesh. In CFD, the dominant discretization method is the Finite Volume Method (FVM), in which the governing equations are integrated over each cell and then equated to a sum of fluxes across its faces via Gauss's theorem. These fluxes, rather than cell-averaged or cell-centered values, are the variables being solved for. The main advantage of FVM is that it is conservative: the flux leaving one cell is automatically equal to the flux entering its neighbor. This is critical in the study of flows, where the conservation of mass, momentum, and energy form the most central principles, [39].

The transport equations of fluids are Partial Differential Equations (PDEs) with several terms. If ψ represents a generic scalar (e.g., temperature), its governing equation could be expressed in the following form,

$$\frac{\partial \rho\psi}{\partial t} + \nabla \cdot (\rho\psi\mathbf{v}) = \nabla \cdot (D_\psi \nabla\psi) + \dot{S}_\psi, \tag{4.1}$$

where $\nabla \cdot (\rho\psi\mathbf{v})$ is a convective term representing transport by the flow velocity $\mathbf{v}$, and $\nabla \cdot (D_\psi \nabla\psi)$ a diffusive term with the diffusion coefficient D_ψ. $\dot{S}_\psi$ represents the sum of source terms, e.g., inter-phase interactions, body forces, or chemical reactions. Each term is typically continuous, which means that linearizing them over discrete steps in time and space induces a discretization error. There are numerous discretization schemes available in the literature, categorized by order of accuracy; a first-order scheme for discretizing space into steps of size Δx has an error of order $\mathcal{O}(\Delta x)$, a second-order scheme has an error of order $\mathcal{O}(\Delta x^2)$, etc. The upwind scheme, [39], a simple first-order scheme for the convective term, has a substantial error that acts as an additional diffusive term, inducing *numerical diffusion*. Higher-order schemes are usually more accurate but may be unbounded, which means that variables that should be bounded between neighboring points can over-shoot or under-shoot, which is a potentially serious error on its own and can cause the solution to diverge. High-order schemes are therefore often implemented as hybrid schemes, which tend toward lower-order accuracy in situations where boundedness cannot be guaranteed, [39].

The governing equations can be discretized and solved as they are. However, if the flow is turbulent, the simulation will not adequately capture the flow physics unless all scales of turbulence are resolved. This requires that the mesh is fine enough and the time step short enough that the Kolmogorov microscales are captured in the simulation. This method is called Direct Numerical Simulation (DNS), a potentially very accurate but extremely computationally expensive approach. DNS is useful for studying small, canonical flows that can easily be meshed with a Cartesian grid. Larger and more complex problems, like combustion in gas turbines, are currently far too demanding. LES solves this problem by allowing coarser grids, leaving the smallest scales of turbulence unresolved. A common criterion for the quality of an LES mesh is that less than 20% of the turbulent kinetic energy is unresolved, [46]. The influence of the unresolved scales is instead accounted for in other ways: "explicit" LES adds source terms to the governing equations, whereas "implicit" LES assumes that discretization has a similar impact to the unresolved scales, [47]. LES with a high-quality mesh is also quite demanding computationally, but modern high-performance computing makes it feasible for many flow problems. A notable challenge in LES is the treatment of turbulent boundary layers, where most of the turbulent kinetic energy belongs to very small scales which necessitates a very fine mesh; the most common solution to this is to use a wall model that leaves the boundary layer largely unresolved while capturing its influence on the bulk flow.

In LES, leaving the smallest scales of turbulence unresolved is mathematically equivalent to applying a spatial low-pass filter to the governing equations, [39]. Let Δ be the filter width. A simple box filter then has the filtering function $G(\mathbf{x}, \mathbf{x}', \Delta)$,

$$\begin{cases} G(\mathbf{x}, \mathbf{x}', \Delta) = 1/\Delta^3 & |\mathbf{x} - \mathbf{x}'| < \Delta/2 \\ G(\mathbf{x}, \mathbf{x}', \Delta) = 0 & |\mathbf{x} - \mathbf{x}'| > \Delta/2, \end{cases} \tag{4.2}$$

where $\mathbf{x}$ is a positional vector in 3D. A box filter is appropriate for high-quality hexahedral meshes, where single mesh cells can act as box filters with Δ computed as the cubic root of the cell volume. The filter is applied to a variable $\psi(\mathbf{x})$ via the convolution

$$\overline{\psi}(\mathbf{x}) = G * \psi = \int_{-\infty}^{\infty} \int_{-\infty}^{\infty} \int_{-\infty}^{\infty} G(\mathbf{x}, \mathbf{x}', \Delta)\psi(\mathbf{x}')\mathrm{d}x_1'\mathrm{d}x_2'\mathrm{d}x_3', \tag{4.3}$$

resulting in the filtered variable $\overline{\psi}$. A tilde instead of an overline symbolizes Favre (i.e., density-weighted) filtering: $\tilde{\psi} = \overline{(\rho\psi)}/\overline{\rho}$. Allowing some variables (typically the ones being solved for) to be Favre-filtered simplifies the filtered governing equations. Applying the filtering operation to eq. 4.1 results in the following equation,

$$\frac{\partial \overline{\rho}\tilde{\psi}}{\partial t} + \nabla \cdot (\overline{\rho}\widetilde{\psi\mathbf{v}}) = \nabla \cdot (\overline{D}_\psi \nabla \tilde{\psi}) + \overline{\dot{S}}_\psi. \tag{4.4}$$

This equation is not particularly useful since $\nabla \cdot (\overline{\rho}\widetilde{\psi\mathbf{v}})$ cannot be described without full information about the unresolved flow field. The convective term is therefore replaced

with one that can be described using only filtered variables, $\nabla \cdot (\overline{\rho}\tilde{\psi}\tilde{\mathbf{v}})$, and the transport equation is re-arranged accordingly,

$$\frac{\partial \overline{\rho}\tilde{\psi}}{\partial t} + \nabla \cdot (\overline{\rho}\tilde{\psi}\tilde{\mathbf{v}}) = \nabla \cdot (\overline{D}_{\psi}\nabla\tilde{\psi}) + \overline{\dot{S}}_{\psi} - \nabla \cdot (\overline{\rho}(\widetilde{\psi\mathbf{v}} - \tilde{\psi}\tilde{\mathbf{v}})). \tag{4.5}$$

Note the new term $\nabla \cdot (\overline{\rho}(\widetilde{\psi\mathbf{v}} - \tilde{\psi}\tilde{\mathbf{v}}))$, which represents the influence of the unresolved scales. In implicit LES, this term is assumed to be similar to the numerical error induced by discretization. In explicit LES, it is approximated using a subgrid model.

4.5 Combustion in CFD

Combustion can be incorporated into a CFD simulation through an auxiliary combustion model. The purpose of the combustion model is to capture the conversion of reactants to products in the inner reaction zone and the heat release associated with this process, typically as source terms in the transport equations for species concentrations and energy.

Flamelet models are a commonly used and computionally efficient family of combustion models, where the progress from reactants to products (both in terms of composition and temperature) is mapped to a single flame progress variable which is solved for using a transport equation, [39]. The main downside of flamelet models is that they rely on strong assumptions about the flame structure, such as the existence of a continuous inner reaction zone. These assumptions are relatively easy to impose for well-defined flames such as premixed flames in the flamelet regime, but challenging for heavily turbulent or partially premixed flames.

A more direct approach is to use Finite Rate Chemistry (FRC), where the CFD simulation is coupled to a chemical reaction mechanism, e.g., HyChem. All species included in the mechanism are separately tracked in the fluid and react with each other at finite rates as modeled by the mechanism. Each mesh cell is typically treated as a single reactor. Because the time scales of individual chemical reactions are much shorter than those of the flow, the evolution of the chemical state in each cell is often integrated separately using operator splitting, [48]. The computational cost of CFD with FRC scales dramatically with the number of species and reactions included in the mechanism, which is why reduced mechanisms such as the HyChem or Zettervall families are necessary.

In LES, the mesh is too coarse to resolve the segmented structure of a flame front. In the simulations presented in this work, the laminar flame width (based on the thermal width) is only covered by one to three cell widths, and the inner reaction zone is thinner than a single cell. The coarseness of the mesh relative to the flame width greatly enhances diffusion between the inner reaction zone and its surroundings, typically resulting in a

very high flame propagation rate. To solve this problem, various Turbulence-Chemistry Interaction (TCI) models can be introduced. An interesting example is the thickened flame model, [49], which artificially increases the flame width by a thickening factor F to make it resolved on the mesh. Mathematically, this involves multiplying the molecular diffusivity by F and dividing reaction rates by F. The Eulerian Stochastic Fields (ESF) model uses another strategy, [50], evolving several iterations of each thermochemical variable (energy and species concentrations), which together form a Probability Density Function (PDF) for the variable. The transport equation for each iteration differs by a stochastic diffusion term representing turbulence-chemistry interaction.

Some TCI models, such as the Eddy Dissipation Concept (EDC) model, [51, 6], do not modify diffusion but instead alter reaction rates (typically by reducing them) based on local turbulence. The EDC model is based on the idea that a turbulent flame front is immersed in a network of vortical fine structures separated by relatively quiescent regions and that chemical reactions occur primarily within the fine structures, [42, 52]. By estimating the volume fraction γ^* of these unresolved fine structures, the LES-filtered reaction rates can be scaled accordingly. The EDC model estimates γ^* through an expression based on the turbulent cascade process with the local turbulent kinetic energy as a parameter. The Fractal Model (FM), [53], estimates γ^* using a different function derived from fractal theory, where the fractal dimension of turbulence and the number of identifiable turbulent scales are taken as parameters. The Partially Stirred Reactor (PaSR) model, [54], which is used here, instead estimates γ^* by comparing the time scales of the chemistry to those of the small-scale turbulence, with short turbulent time scales increasing γ^*. The name alludes to the Perfectly Stirred Reactor (PSR) model, which simply assumes that $\gamma^* = 1$.

With the necessary theoretical background established, the next chapter concisely presents the equations, models, and assumptions used in this work specifically.

Chapter 5

Methodology

This chapter describes the LES methodology used in this work.

5.1 Governing equations and closure models

The governing equations are:

$$\begin{cases} \dfrac{\partial \overline{\rho}}{\partial t} + \nabla \cdot (\overline{\rho}\tilde{\mathbf{v}}) = \overline{\dot{\rho}_l}, & \text{(5.1a)} \\ \dfrac{\partial \overline{\rho}\tilde{\mathbf{v}}}{\partial t} + \nabla \cdot (\overline{\rho}\tilde{\mathbf{v}} \otimes \tilde{\mathbf{v}}) = -\nabla \overline{p} + \nabla \cdot \overline{\boldsymbol{\tau}} + \overline{\mathbf{f}_l} - \nabla \cdot \mathbf{B}, & \text{(5.1b)} \\ \dfrac{\partial \overline{\rho}\tilde{H}_K}{\partial t} + \nabla \cdot (\overline{\rho}\tilde{H}_K\tilde{\mathbf{v}}) = \dfrac{\partial \overline{p}}{\partial t} + \nabla \cdot (\overline{\boldsymbol{\tau}}\tilde{\mathbf{v}}) + \nabla \cdot (\overline{\alpha}\nabla\tilde{h}) + \overline{\dot{q}_c} + \overline{\dot{q}_l} - \nabla \cdot \mathbf{b}_E, & \text{(5.1c)} \\ \dfrac{\partial \overline{\rho}\tilde{Y}_i}{\partial t} + \nabla \cdot (\overline{\rho}\tilde{Y}_i\tilde{\mathbf{v}}) = \nabla \cdot (\overline{D_i}\nabla\tilde{Y}_i) + \overline{\dot{\omega}_i} + \overline{\dot{\rho}_{il}} - \nabla \cdot \mathbf{b}_i. & \text{(5.1d)} \end{cases}$$

Equations 5.1a, 5.1b, 5.1c, and 5.1d are filtered transport equations for mass, momentum, energy, and species concentrations, respectively. Here, h represents sensible enthalpy and $\tilde{H}_K = \tilde{h} + \frac{1}{2}|\tilde{\mathbf{v}}|^2$. $\tilde{Y}_i$ is the mass fraction of species i, and each species under consideration has a transport equation like eq. 5.1d. The fluid is assumed to be Newtonian and the Stokes hypothesis is applied, [39], such that the filtered viscous stress tensor is given by the relation $\overline{\boldsymbol{\tau}} = 2\overline{\mu}\tilde{\mathbf{D}} - \frac{2}{3}\overline{\mu}(\nabla \cdot \tilde{\mathbf{v}})\mathbf{I}$, where the filtered strain rate tensor is given by $\tilde{\mathbf{D}} = \frac{1}{2}(\nabla\tilde{\mathbf{v}} + \nabla\tilde{\mathbf{v}}^T)$.

The diffusive terms $\nabla \cdot (\overline{\alpha}\nabla\tilde{h})$ and $\nabla \cdot (\overline{D_i}\nabla\tilde{Y}_i)$ are based on Fourier heat conduction and Fickian diffusion, respectively, with thermal and species diffusivities denoted $\overline{\alpha}$ and

$\overline{D_i}$. Sutherland's law (with coefficients for dry air) is used to compute $\overline{\mu}$ and $\overline{\alpha}$. A unity Schmidt number is assumed for all species such that $\overline{D_i} = \overline{\mu}$. The diffusive terms could be modeled more accurately by differentiating between different species and species pairs, but since turbulent diffusion is expected to dominate over molecular diffusion in the cases studied here, this added complexity is likely not warranted.

The effects of the unresolved scales are accounted for by the subgrid terms $\nabla \cdot \mathbf{B}$, $\nabla \cdot \mathbf{b}_E$, and $\nabla \cdot \mathbf{b}_i$. This work uses a functional subgrid model, which means that these take the form of diffusive terms proportional to the subgrid viscosity ν_{sgs}, following Boussinesq's hypothesis, [39]. The terms are thus modeled as,

$$\begin{cases} \mathbf{B} = 2\overline{\rho}\left(-\nu_{sgs}\tilde{\mathbf{D}}_D + \frac{1}{3}k\mathbf{I}\right), & \text{(5.2a)} \\ \mathbf{b}_E = -\overline{\rho}\frac{\nu_{sgs}}{\mathrm{Pr_T}}\nabla\tilde{h}, & \text{(5.2b)} \\ \mathbf{b}_i = -\overline{\rho}\frac{\nu_{sgs}}{\mathrm{Sc_T}}\nabla\tilde{Y}_i, & \text{(5.2c)} \end{cases}$$

where $\tilde{\mathbf{D}}_D$ is the deviatoric part of the strain rate tensor. The turbulent Prandtl and Schmidt numbers, $\mathrm{Pr_T}$ and $\mathrm{Sc_T}$, are constant and set to 0.85 and 1, respectively (except in paper III, where $\mathrm{Pr_T} = 1$). Close to solid walls, ν_{sgs} is adjusted according to Spalding's law of the wall, [55], to capture the effects of the unresolved boundary layer. Otherwise, ν_{sgs} is computed from the subgrid kinetic energy k via the relation $\nu_{sgs} = C_k\sqrt{k}\Delta$, where the LES filter width Δ is locally equated to the cubic root of each mesh cell. The Localized Dynamic K-equation Model (LDKM), [56], is used to compute k, which involves solving an additional transport equation,

$$\frac{\partial\overline{\rho}k}{\partial t} + \nabla\cdot(\overline{\rho}k\tilde{\mathbf{v}}) = -\mathbf{B}\cdot\tilde{\mathbf{D}} + \nabla\cdot((\overline{\mu} + \overline{\rho}\nu_{sgs})\nabla k) - C_\epsilon\frac{\overline{\rho}k^{3/2}}{\Delta}, \qquad (5.3)$$

where the model coefficients C_ϵ and C_k are computed dynamically. The LDKM model is based on the simpler One-Equation Eddy Viscosity Model (OEEVM), [57], which uses constant coefficients obtained from an analysis of the turbulent energy cascade.

The filtered chemical reaction rate of species i is denoted $\overline{\dot{\omega}_i}$ and the associated net heat release rate is obtained from the relation $\overline{\dot{q}_c} = \sum_{i=1}^{N} h_i^\theta\overline{\dot{\omega}_i}$, where h_i^θ is the formation enthalpy. The filtered reaction rates, which depend on subgrid turbulence-chemistry interaction, are closed using the PaSR model, [54], such that $\overline{\dot{\omega}_i} = \gamma^*\dot{\omega}_i$ where $\dot{\omega}_i$ is the unfiltered reaction rate based on perfect subgrid mixing. The fine structure volume fraction γ^* acts as a scaling factor and is approximated using the expression $\gamma^* = \tau_c/(\tau_c + \tau_m)$, where τ_c and τ_m are representative time scales for chemistry and small-scale turbulent mixing, respectively. The mixing time scale describes the behavior of the turbulent fine structures, which are on the order of the Kolmogorov time scale τ_K. Some PaSR codes equate τ_m

and τ_K, but this treatment neglects the anisotropy of the fine structures (which are shaped like sheets and ribbons, [42]) since τ_K describes isotropic turbulence. Here, the PaSR formulation uses the geometric mean $\sqrt{\tau_K \tau_\Delta}$, where τ_Δ is the time scale of subgrid velocity stretch, defined by the relation $\tau_\Delta = k^{-1/2}\Delta$. The chemical time scale is assumed constant and equated to δ_u/s_u, where δ_u is the laminar flame width.

Both s_u and δ_u are extracted *a priori* from 1D laminar flame simulations. In premixed flames (case A), τ_c is well-defined and constant throughout the flame. In partially premixed flames (case B), τ_c theoretically varies from point to point based on the local z, but the stoichiometric value is assumed to be representative as it corresponds to the propagation rate of the leading edge in a triple flame. Using a constant τ_c reduces complexity by allowing turbulence-chemistry interaction to be entirely turbulence-driven. On the other hand, it does not account for substantially varying z, nor reactions far away from the inner reaction zone, such as the gradual approach towards chemical equilibrium in the postflame zone of a premixed flame. Because of these downsides, I recommend the use of a dynamic τ_c model, e.g., [58], in future simulation studies. Note that δ_u is computed slightly differently in the papers included in this thesis: in papers I-III, it is estimated as ν/s_u, where ν is the kinematic viscosity of the unburnt air, whereas in papers IV-V it is obtained directly from the laminar flame simulations as the thermal thickness. Both methods are theoretically sound, but the latter gives a stronger flame, which was found to improve the simulation accuracy in case B.

5.2 Spray modeling

The terms $\overline{\dot{\rho}_l}$, $\overline{\mathbf{f}_l}$, $\overline{\dot{q}_l}$, and $\overline{\dot{\rho}_{il}}$ represent spray-gas transfer of mass, momentum, energy, and species concentrations. These are ignored in case A, where there is no spray. The spray itself is a dispersed cloud of microscopic droplets, one to three orders of magnitude smaller than Δ, which makes the liquid phase difficult to track with the same Eulerian approach used for the continuous gas phase. The standard practice is to instead use a Lagrangian model where the spray is represented by a cloud of statistical particles, [59], often called parcels since they represent groups of identical droplets, [60]. The evolution of the particles is integrated separately from that of the Eulerian phase, necessitating a sufficiently short time step to accurately capture inter-phase interactions. The evolution of a particle is governed

by the equations,

$$\begin{cases} \dfrac{d\mathbf{x}_p}{dt} = \mathbf{v}_p, & \text{(5.4a)} \\ \dfrac{d\mathbf{v}_p}{dt} = \dfrac{f}{\tau_v}(\tilde{\mathbf{v}} - \mathbf{v}_p) + \mathbf{g}, & \text{(5.4b)} \\ \dfrac{dm_p}{dt} = -\dot{m}_{vap}, & \text{(5.4c)} \\ \dfrac{dd_p}{dt} = -\dot{d}_{vap} - \dot{d}_{br}, & \text{(5.4d)} \\ \dfrac{dT_p}{dt} = \dfrac{h_{conv}\pi d_p^2(\tilde{T} - T_p) - \dot{m}_{vap}\Delta H_{vap}}{m_p c_{p,p}}, & \text{(5.4e)} \end{cases}$$

where $\mathbf{x}_p$, $\mathbf{v}_p$, m_p, d_p, and T_p represent the particle position, velocity, mass, diameter, and temperature, respectively, whereas $\tilde{T}$ is the filtered temperature of the gas phase. The particles are assumed to be spherical: $m_p = \frac{1}{6}\rho_p \pi d_p^3$. The gravitational acceleration vector is denoted $\mathbf{g}$. The density ρ_p, specific heat capacity $c_{p,p}$, and heat of vaporization ΔH_{vap} are functions of temperature specified in the liquid model. The drag factor is defined as $f = \frac{1}{24} C_D \mathrm{Re}_p$ and represents the ratio between the drag coefficient and the Stokes drag, [61]. The particle relaxation time is defined by the equation $\tau_v = \rho_p d_p^2 / 18(\overline{\mu} + \overline{\rho}\nu_{sgs})$. The drag coefficient is computed from the particle Reynolds number Re_p using the following relation, which assumes spherical droplets:

$$\begin{cases} C_D = \frac{24}{\mathrm{Re}_p}\left(1 + \frac{1}{6}\mathrm{Re}_p^{\frac{2}{3}}\right), & \mathrm{Re}_p \leq 1000 \\ C_D = 0.424. & \mathrm{Re}_p > 1000 \end{cases} \tag{5.5}$$

The droplet diameter changes over time due to vaporization, represented by $\dot{d}_{vap}$, but also due to secondary breakup, represented by $\dot{d}_{br}$. The Reitz-Diwakar model, [62], which accounts for breakup in the bag and stripping modes, is used to calculate $\dot{d}_{br}$. The breakup rate is given by,

$$\dot{d}_{br} = \frac{d_p - d_{stable}}{\tau_{br}}, \tag{5.6}$$

where d_p is a stable diameter and τ_{br} the breakup time. If the droplet Weber number We is smaller than or equal to C_{bag}, $\dot{d}_{br} = 0$. If $C_{bag} < \mathrm{We} \leq C_{strip}\sqrt{\mathrm{Re}_p}$, breakup occurs in the bag mode. The model coefficients C_{bag} and C_{strip} are set to 6 and 0.5, respectively. In the bag mode, the following equations are used,

$$\begin{cases} d_{stable} = 2C_{bag}\dfrac{\sigma_p}{\overline{\rho}|\tilde{\mathbf{v}} - \mathbf{v}_p|^2}, & \text{(5.7a)} \\ \tau_{br} = C_{bag} d_p \sqrt{\dfrac{\rho_p d_p}{\sigma_p}}, & \text{(5.7b)} \end{cases}$$

where σ_p and ρ_p are the surface tension and density of the liquid phase. The breakup mode changes to stripping when $\mathrm{We} > C_{strip}\sqrt{\mathrm{Re}_p}$, and the following equations are used instead,

$$\begin{cases} d_{stable} = 4C_{strip}^2 \dfrac{\sigma_p^2}{\overline{\rho}\,(\overline{\mu} + \overline{\rho}\nu_{sgs})|\tilde{\mathbf{v}} - \mathbf{v}_p|^3}, & \text{(5.8a)} \\ \tau_{br} = \dfrac{C_{strip} d_p}{|\tilde{\mathbf{v}} - \mathbf{v}_p|}\sqrt{\dfrac{\rho_p}{\overline{\rho}}}. & \text{(5.8b)} \end{cases}$$

When the diameter changes, the number of droplets n in each particle is adjusted to maintain its mass.

Using the model developed by Zuo *et al.*, [63], the calculation of the vaporization rate $\dot{m}_{vap}$ is carried out differently depending on whether T_p is below or at the pressure-dependent boiling temperature T_{boil}. If $T_p < T_{boil}$, the following relation is used,

$$\dot{m}_{vap} = \pi d_p \rho_s D_s \mathrm{Sh}_p \ln\left[1 + B_M\right], \tag{5.9}$$

where ρ_s is the droplet surface density and D_s the vapor diffusivity of the fuel. The surface density is computed via the ideal gas law at the droplet surface. Sh_p and B_M represent the droplet Sherwood number and Spalding mass transfer number, respectively.

If $T_p \geq T_{boil}$, the following equation is used for the vaporization rate,

$$\dot{m}_{vap} = \dot{m}_{flash} + \dot{m}_t, \tag{5.10}$$

where $\dot{m}_{flash}$ models superheated flash boiling and $\dot{m}_t$ vaporization due to external heat transfer. The first term is computed by the relation,

$$\dot{m}_{flash} = \pi d_p^2 h_{flash} \frac{T_p - T_{boil}}{\Delta H_{vap}}, \tag{5.11}$$

where the heat transfer coefficient h_{flash} increases with temperature following an empirical correlation. The vaporization due to external heat transfer is calculated iteratively as,

$$\dot{m}_t = \pi d_p \overline{\alpha}\,\overline{\rho} \frac{\mathrm{Sh}_p}{1 + \dot{m}_{flash}/\dot{m}_t} \ln\left[1 + \frac{\tilde{h} - h_s}{\Delta H_{vap}}\left(1 + \frac{\dot{m}_{flash}}{\dot{m}_t}\right)\right], \tag{5.12}$$

where h_s is the surface enthalpy of the fuel.

The convective heat transfer coefficient h_{conv} is obtained from the particle Nusselt number Nu_p:

$$h_{conv} = \frac{\overline{\rho}\,\overline{\alpha}\,\overline{c_p}}{d_p}\mathrm{Nu}_p. \tag{5.13}$$

Note that the Nusselt number is usually expressed using thermal conductivity, which is equivalent to $\overline{\rho}\,\overline{\alpha}\,\overline{c_p}$. Both the Nusselt number and the Sherwood number (used for vaporization) are provided by the Ranz-Marshall model, [64], for turbulent interphase diffusion,

$$\begin{cases} \mathrm{Nu}_p = 2 + 0.6\mathrm{Re}_p^{\frac{1}{2}}\mathrm{Pr}_g^{\frac{1}{3}}, & \text{(5.14a)} \\ \mathrm{Sh}_p = 2 + 0.6\mathrm{Re}_p^{\frac{1}{2}}\mathrm{Sc}_g^{\frac{1}{3}}, & \text{(5.14b)} \end{cases}$$

where Pr_g and Sc_g are the Prandtl and Schmidt numbers of the gas phase.

After the governing equations for the Lagrangian phase (eq. 5.4a-5.4e) have been updated, the source terms for the Eulerian phase are calculated as,

$$\begin{cases} \overline{\dot{\rho}_l} = \dfrac{1}{dV}\displaystyle\sum_{j=1}^{J} n_j[\dot{m}_{vap,j}], & \text{(5.15a)} \\ \overline{\mathbf{f}_l} = \dfrac{1}{dV}\displaystyle\sum_{j=1}^{J} n_j\Big[\dot{m}_{vap,j}\mathbf{v}_{p,j} - m_{p,j}\dfrac{f}{\tau_v}(\tilde{\mathbf{v}} - \mathbf{v}_p)\Big], & \text{(5.15b)} \\ \overline{\dot{q}_l} = \dfrac{1}{dV}\displaystyle\sum_{j=1}^{J} n_j\Big[\dot{m}_{vap,j}\Delta H_{vap,j} - h_{conv,j}\pi d_{p,j}^2(\tilde{T} - T_{p,j})\Big], & \text{(5.15c)} \\ \overline{\dot{\rho}_{il}} = \dfrac{1}{dV}\displaystyle\sum_{j=1}^{J} n_j[\dot{m}_{vap,i,j}], & \text{(5.15d)} \end{cases}$$

where dV is a control volume (i.e., mesh cell) containing J particles with n_j droplets each. Particles passing through the same mesh cell also exchange momentum via a stochastic collision model, [65]. Here, the source term $\overline{\dot{\rho}_{il}}$ is zero for all species i except the fuel species since only that species is present in the liquid. If the liquid contains multiple species, individual vaporization terms $\dot{m}_{vap,i}$ are computed. The net vaporization rate $\dot{m}_{vap}$ is the sum of all species vaporization rates, and all parameters that are influenced by liquid properties, e.g., τ_v, τ_{br}, and h_{conv}, are computed as weighted averages across all species in the liquid. Because different species may be vaporized at different rates, the mass fraction of each species must also be updated when evolving the Lagrangian phase.

5.3 Numerical methods

The governing equations of the Eulerian phase, the Lagrangian phase, and the chemistry are solved separately using operator splitting. The Lagrangian equations thus become Ordinary Differential Equations (ODEs) integrated in time using the implicit Euler scheme.

The chemistry equations consist of one ODE per species describing its production or consumption rate $\dot{\omega}_i$, which is influenced by the concentration of all species with which it can react. In paper III (the earliest study chronologically), the equation system is integrated in time using a Rosenbrock scheme, but this was later found to produce mass and energy conservation errors. It was therefore replaced by the *seulex* algorithm, [66], an extrapolation method based on the implicit Euler scheme, in the remaining papers. The Eulerian equations are PDEs that require both temporal and spatial discretization. The first-order implicit Euler scheme is used for temporal discretization, as it was found to be both robust and accurate for the relatively short time steps used in the LES.

The convective and diffusive terms are expressed as fluxes at the cell faces, computed using interpolated variables from the neighboring cell centers. Diffusive fluxes are discretized using second-order central differencing, with orthogonal correction when the cell face normal is not aligned with the two neighboring cell centers. Convective fluxes are discretized using the *gamma* scheme, [67], a weighted blend between first-order upwind differencing and second-order central differencing. For a generic scalar ψ, the blending function is determined by the gradient ratio $(\psi_D - \psi_U)/(2(\nabla\psi)_U \cdot \mathbf{d})$, where ψ_D and ψ_U are the nodal values of ψ at the downstream and upstream cell centers, $(\nabla\psi)_U$ is the gradient of ψ at the upstream cell center, and $\mathbf{d}$ is a unit vector aligned with the cell centers. The cell-centered gradient $(\nabla\psi)_U$ is computed using the least-squares method based on ψ in the neighboring cell centers. If the gradient ratio is greater than one or has a negative sign, central differencing risks becoming unbounded and upwind differencing is used. If the gradient ratio is 0.5 or smaller, the central differencing scheme is considered bounded and is used fully. If the gradient ratio is between 0.5 and 1, a blend of the two schemes is used to maintain stability.

The momentum equation (eq. 5.1b) contains both velocity and pressure, two quantities that are intimately coupled in fluid mechanics. These must be artificially decoupled for the equation to become numerically solvable in a compact linear equation system. Here, the Pressure Implicit Splitting of Operators (PISO) decoupling algorithm is used, [68], in which the momentum equation is split into separate equations. First, velocity is predicted using the last known pressure. The predicted velocity is then used as a constant in a pressure correction equation to calculate a new pressure consistent with the predicted velocity. The consistency is not mutual, however, which means that the velocity must also be corrected based on the new pressure. This iterative sequence of solutions is called a pressure correction loop and is performed three times in the present work to ensure acceptably low residuals.

For each time step in the simulation, from t_n to t_{n+1}, the following steps are carried out:

1. If it exists, the Lagrangian phase is evolved to t_{n+1}, and the source terms based on its contribution to the Eulerian phase are calculated.

2. The continuity equation is solved for mass fluxes.
3. The momentum equation is solved for (predicted) velocity fluxes.
4. The chemical source terms $\overline{\dot{\omega}_i}$ are computed by the chemical integration scheme and corrected by the PaSR model.
5. The species equations are solved for species fluxes.
6. The energy equation is solved for energy fluxes.
7. Thermodynamic variables directly determined by composition and temperature are updated, e.g., $\overline{\mu}$ and $\overline{\alpha}$.
8. The pressure correction loop ensures consistency between pressure and velocity.
9. Equation 5.3 is solved for the subgrid kinetic energy fluxes. The turbulent viscosity is updated.

The density is recalculated using the ideal gas law several times: after the temperature has been updated, after the pressure is corrected, and at the end of the loop.

All equations are discretized and solved using the open-source OpenFOAM 7 C++ library, [69]. The *reactingFoam* solver is used for case A, and the *sprayFoam* solver is used for case B. These solvers are theoretically equivalent in the absence of a spray.

Chapter 6

Cases

This chapter describes the two simulation cases studied in this work.

6.1 Case A: The Cambridge bluff body burner

Case A is a premixed bluff body burner studied experimentally by Pathania *et al.*, [7], with Jet A, C1, ethanol, and n-heptane. A schematic of the burner is shown in Fig. 6.1(a). A lean mixture of air and vaporized fuel at 393 K flows upward through an annular pipe and past a conical bluff body with a diameter D of 23 mm, discharging with a bulk velocity U_b of 23.5 m/s into an unconfined space at ambient conditions. The burner is entirely axisymmetric. The bluff body wake contains an RZ of reversed flow, allowing a flame to stabilize at the shear layer between it and the main flow. The equivalence ratios are 0.82 for Jet A, 0.85 for C1, 0.75 for ethanol, and 0.75 for n-heptane; all of these values are 20% higher than the lowest stable ϕ for each fuel. Experiments were also carried out near blow-off, but they are not considered in this work. Physical measurements included Planar Laser-Induced Fluorescence (PLIF) for non-quantitative OH and CH_2O images, and particle image velocimetry for quantitative velocity images. Image processing algorithms were then used to extract further quantitative data such as the mean progress variable $\langle c \rangle$ and the integral length scale of turbulence L_T. Some of these post-processing techniques are repeated on the simulation data in paper I for a thorough validation against the experiments. A new parameter, the flame sheet diameter D_f, is also introduced: it is computed at a specific y (height above the bluff body) by binarizing a central cut of the OH distribution by its 20% contour, then computing the area of the above-threshold region within a thin rectangle centered on y and dividing by the rectangle width. By computing D_f for each available snapshot of the OH distribution, its mean $\langle D_f \rangle$ and standard deviation $\mathrm{std}(D_f)$ are ob-

tained; the former is an indicator of the flame size and the latter a quantifier of fluctuations in the flame surface.

The computational domain for case A is shown in Fig. 6.1(b). A fixed mass flux inlet $3.9D$ upstream of the pipe exit is immediately followed by two gratings that trigger a turbulent transition on the resolved scales. The turbulent flow develops as it travels through the pipe, then discharges into a cylindrical space $7.8D$ in diameter. The cylindrical space is $8.5D$ long and ends with an adiabatic, zero-gradient velocity plane. A wave-transmissive condition is used for pressure to avoid wave reflection. The same boundary conditions are used for the side boundaries. The bottom boundary, which is parallel to the pipe exit, has a fixed normal velocity of 1 m/s representing ambient co-flow around the flame. All solid boundaries are treated as adiabatic no-slip surfaces. The domain is discretized using a block-structured hexahedral mesh as shown in Fig. 6.1(b). The baseline mesh used in this work has 16.8M cells and a $\Delta = 0.25$ mm in the flame, but other resolutions are also used to investigate mesh sensitivity. The baseline mesh is locally refined in the main region of interest, which begins in the middle of the pipe section and ends downstream of the RZ.

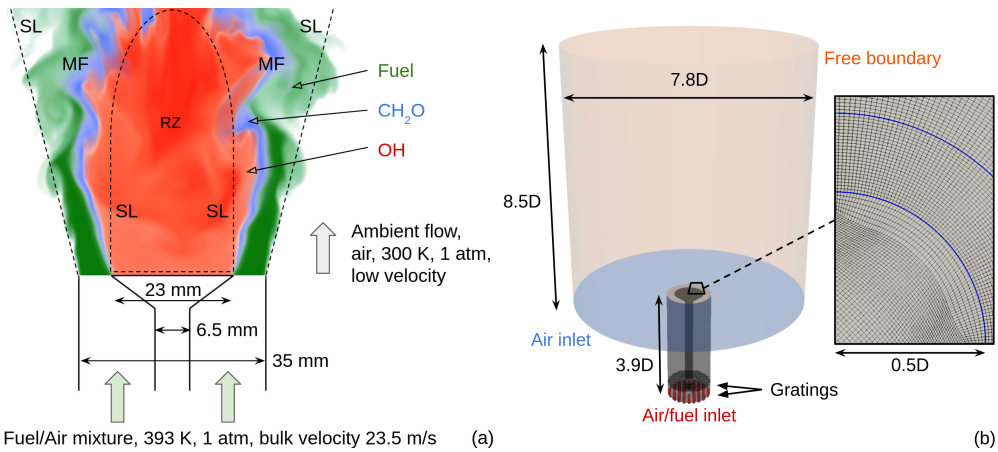

Figure 6.1: Schematic of case A (a) and the computational domain (b). The mesh is shown in a slice just above the bluff body, with the edges of the bluff body and pipe in blue. SL = Shear Layer. MF = Main Flow.

Case A is chosen for this work for two reasons: the existence of detailed experimental data for Jet A and C1 (which is not widely available), and its simplicity. The simplicity of the case makes it highly useful for model validation and investigating the sensitivity to mesh resolution and model choice. It also allows for a quantitative comparison of the fundamental flame dynamics of the different fuels, such as their flame sheet width, preheat layer thickness, and flame surface density.

6.2 Case B: The DLR single-cup spray combustor

Case B is a single-cup spray combustor at the German Aerospace Center (DLR), studied experimentally by Meier *et al.*, [8], with Jet A. With prefilming airblast atomization and swirl stabilization, the rig is intended to be a generic representative of real jet engine combustors but with optical access to enable measurements. Two operating conditions were studied, representing idle (4 bar) and cruise (10 bar) conditions. The flame and postflame zone were visualized using OH chemiluminescence and OH-PLIF imaging. Detailed spray statistics were extracted using phase Doppler anemometry. A cutaway of the combustor (or more specifically the simulation domain) is shown in Fig. 6.2. Preheated main air is supplied through a plenum to a burner containing two sets of co-rotating swirlers. Liquid fuel is injected as a film along the prefilmer lip, the final section of the inner burner wall, and atomized between the co-rotating air flows at the end of the lip. This creates a spray shaped like a hollow cone, carried by the airflow into the combustion chamber while rapidly heated and vaporized. Due to the rotation of the gas flow and the sudden expansion of the combustion chamber, a Central Recirculation Zone (CRZ) forms downstream of the burner via vortex breakdown. The cone of axial flow surrounding the CRZ is referred to as the main flow cone. The combustion reactions primarily occur in the vicinity of the inner shear layer between the CRZ and main flow cone, although there is a substantial amount of activity in the main flow cone as well. There is also an Outer Recirculation Zone (ORZ), which is partly fed by combustion products from the main flow cone and partly by a cooling film along the combustor walls. The CRZ ends approximately halfway through the combustion chamber, beyond which the flow is entirely axial. The combustion chamber ends with a converging exit nozzle. All operating conditions are given in Table 6.1.

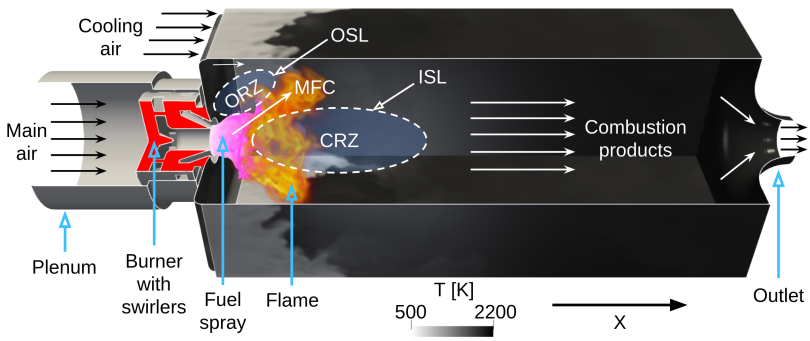

Figure 6.2: Cutaway of case B. The solid sections of the burner are shown in red and the walls are colored by temperature. MFC = Main Flow Cone. OSL = Outer Shear Layer. ISL = Inner Shear Layer.

The computational domain is discretized using a block-structured hexahedral mesh with 6.0M cells and Δ between 0.33 and 0.5 mm in the near-flame region. The velocity and temperature at the plenum and cooling slot boundaries match Table 6.1, and the pressure

Table 6.1: Operating conditions as reported by Meier *et al.*, [8].

	Idle	Cruise
Air pressure [MPa]	0.4	1.0
Air preheat temperature [K]	550	650
Burner pressure loss [%]	3	3
Burner air mass flux [g/s]	60	140
Cooling air mass flux [g/s]	17	39
Liquid fuel mass flux [g/s]	3.0	6.8

is specified at the outlet as part of a wave-transmissive boundary condition. All walls, including the fuel injection slot, are treated as adiabatic no-slip walls. The adiabaticity assumption is not trivial, as neglecting heat losses to the walls (and via radiation) may cause an overestimation of the ORZ temperature, which in turn affects the size of the CRZ. However, Agostinelli *et al.*, [70], demonstrated that the acoustic response of the combustor may be heavily affected by the choice of thermal boundary condition, making an adiabatic condition preferable as it simplifies the analysis.

The spray is introduced at the prefilmer lip, fully atomized, as a cloud of Lagrangian particles. In paper III, the particles are injected axially just upstream of the prefilmer lip. This creates a dense region of particles along the lip, acting as a quasi-film. The particle size distribution is the same as the one proposed by Jones *et al.*, [71], based on experimental measurements. This injection method results in a very narrow and overly concentrated spray propagating almost entirely axially into the combustion chamber. The liquid fuel moves slowly along the prefilmer lip, causing the total liquid mass there to grow large. The amount of liquid at the lip is heavily affected by the pressure gradient into the combustion chamber, facilitating strong coupling between the vaporization rate (and by extension the heat release rate) and the combustor pressure, which causes very strong thermoacoustic oscillations with amplitudes up to $\sim$7% of the combustor pressure. To resolve these issues, in papers IV and V, the injection method is changed to be more explicitly based on experimental measurements. The injection point (or more exactly, ring) is moved just downstream of the prefilmer lip, and dispersion is introduced by assigning random injection directions to each droplet within $\pi/3$ of the axial direction. This formulation was found by iteration with experimentally measured spray statistics as a target, and naturally led to superior agreement with the experiments at the cost of neglecting the film entirely. The initial droplet size distribution produced by atomization depends on the liquid properties of the fuel, in particular ρ, μ, and σ. To account for this, the size distribution is slightly shifted towards smaller or larger droplets based on the mean Sauter Mean Diameter (SMD) predicted by Lefebvre's correlation for airblast atomization, [72], relative to the SMD predicted for Jet A.

Chapter 7

Results

This chapter highlights the most important results from the simulations and, where applicable, connects them to the underlying properties of the fuels.

7.1 Mesh sensitivity

The LES filter width Δ is based on cell volumes and therefore directly tied to the mesh resolution. This means that the mesh resolution not only affects the discretization error, as in all numerical simulations, but also the governing equations themselves by determining how much of the turbulent energy cascade is resolved or unresolved. It is crucial to assess the impact of mesh resolution on the simulation results before they are analyzed further. Figure 7.1 shows the normalized OH distribution for Jet A in case A (a) and case B (b) across a range of meshes. The OH distribution is appropriate for this purpose, being a crucial intermediate species in the combustion process that is also diffusive enough to be easily compared across different resolutions.

Four meshes were designed for case A, ranging from 4.2M to 27.7M cells. The two coarser meshes produce relatively small and weak flames, whereas the finer meshes produce larger and more stable flames. There appears to be a critical resolution threshold between the second and third mesh, which correspond to $\delta_u/\Delta = 1.1$ and $\delta_u/\Delta = 1.5$, respectively. Not only the overall flame size is affected by this threshold, but also the Heat Release Rate (HRR) next to the rim of the bluff body. Since the simulated flames are virtually stationary at that location, regardless of mesh resolution, it appears that a certain resolution level must be reached to ensure that the subgrid reaction rates are predicted correctly. A similar threshold is observed for all fuels, but the finest mesh is reserved for Jet A. The remainder of the results in this thesis are obtained with the 16.8M cell mesh.

For case B, the base mesh consists of 6M cells. Refining it uniformly in all three spatial directions increases the cell count eightfold, resulting in a fine mesh with 48M cells. The finer mesh is prohibitively expensive to use, which is why it is limited to a single simulation at idle conditions. Refining the mesh has a noticeable impact on the results, making the flame more compact and bringing it closer to the spray. This is the result of a higher local HRR, as in case A. The magnitude of the difference is small enough to make the base mesh acceptable for its intended purpose, which is to capture the difference between the flames of different fuels. As demonstrated for case A in paper I, the mesh requirements for Jet A and C1 appear identical.

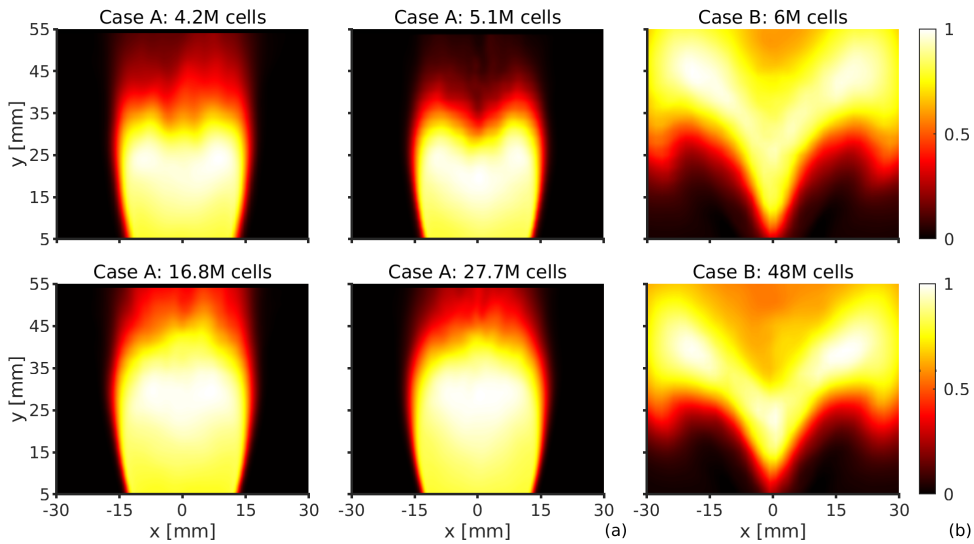

Figure 7.1: Normalized OH distribution for four mesh resolutions in case A (a) and two mesh resolutions in case B (b).

7.2 Reaction mechanism sensitivity

The two families of chemical reaction mechanisms used in this thesis, HyChem and Z79, are different in many respects. Although they use the same surrogate fuel molecules, they have different numbers of intermediate species and reactions, make different predictions of s_u, τ_{ign}, and K_{ext}, and were developed differently. Their predictions in LES likely also differ, and the magnitude of this difference is investigated here.

Figure 7.2(a) shows the normalized CH_2O distribution in case A for Jet A, JP-5, C1, and C5 when using HyChem versus Z79. The HyChem mechanisms all predict relatively similar flames, whereas the Z79 flames are more diverse. The difference between HyChem and Z79 is negligible for Jet A, small for JP-5, large for C1, and very large for

C5, with the Z79 mechanisms consistently predicting smaller flames. The relative difference in maximum mean flame diameter, $\langle D_{f,Z79}\rangle/\langle D_{f,HyChem}\rangle$, is plotted for each fuel in Fig. 7.2(b) as a function of the corresponding relative difference in laminar temperature ratio $\mathrm{TR}_{L,Z79}/\mathrm{TR}_{L,HyChem}$. TR_L is computed from laminar flame simulations as $(T_b - T_u)/T_u$, where T_b and T_u are the temperatures of the burnt and unburnt gas, respectively. Results from ethanol and n-heptane are also included. (Ethanol is simulated using Z74, which is closely related to Z79.) Ethanol and heptane are not included in the HyChem family, so the mechanisms of Pichler *et al.*, [73], and Zeuch *et al.*, [74], are used to obtain these data points instead. The relative flame size in the LES appears to be closely correlated with the relative laminar flame temperature. This is highly useful because it suggests that the behavior of different reaction mechanisms can be predicted *a priori*.

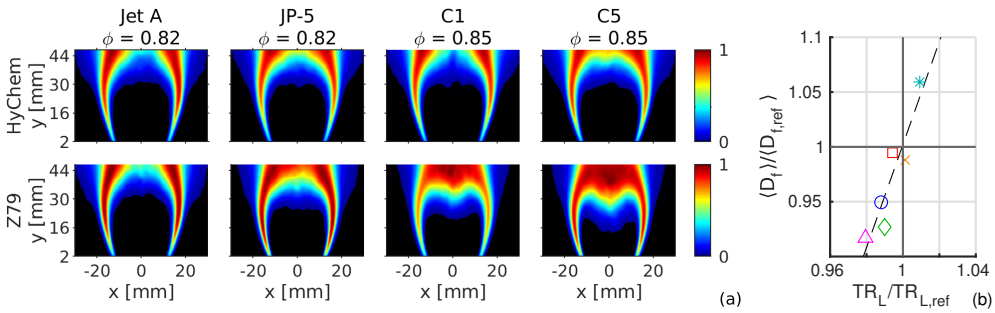

Figure 7.2: CH_2O distribution in case A with the HyChem and Z79 mechanisms (a) and the relative flame width for each fuel plotted against the relative laminar temperature ratio (b). (The reference mechanisms for ethanol, [73], and n-heptane, [74], are not from the HyChem family.) Legend: Jet A (red square), JP-5 (blue circle), C1 (green diamond), C5 (magenta triangle), ethanol (cyan star), n-heptane (orange cross).

The reason for the considerable difference between the predictions of the HyChem and Z79 mechanisms lies in the base chemistry of Z79, which is identical for all fuels bar a single exception: the rates of reactions involving the hydrogen radical H are tweaked to achieve accurate predictions of s_u and τ_{ign}. As shown in the next section, replacing the base chemistry of JP-5, C1, and C5 with that of Jet A gives a set of results that are considerably more similar to each other and the HyChem predictions. I do not consider this tweak advisable, however, as it has an adverse effect on the more fundamental flame parameters s_u and τ_{ign}, the accuracy of which underpins the entire simulation methodology.

7.3 Premixed flame characteristics

Figure 7.3 shows the instantaneous and time-averaged CH_2O distributions in a central cut through the case A flame, as predicted by the HyChem mechanisms. Each panel is normalized separately by its highest value. CH_2O forms close to the reaction zone and diffuses into

the preheat zone, making the CH_2O distribution an indicator of the preheat zone. Only the simulations with the HyChem mechanisms are shown. Comparing the instantaneous distributions with the experimental CH_2O-PLIF images, it is clear that the simulations reproduce the turbulent structures of the preheat zone quite well; small eddies form near the anchoring point and are stretched and expanded as they move upward. However, while the experiments show fine structures immediately after the anchoring point ($y = 2$ mm), the simulated flame is practically stationary there, with the first eddies forming at $y \sim 10$ mm. This can be attributed to Δ, which is too large to resolve the smallest scales of turbulence. Better agreement could be achieved by locally refining the mesh in this region and making the pipe model less idealized (e.g., by introducing surface roughness), but this would likely be a waste of effort and computational time since the simulations are quite accurate beyond $y \sim 10$ mm. For Jet A and C1, the time-averaged CH_2O distributions agree very well with the experimental data. For further validation, see paper I.

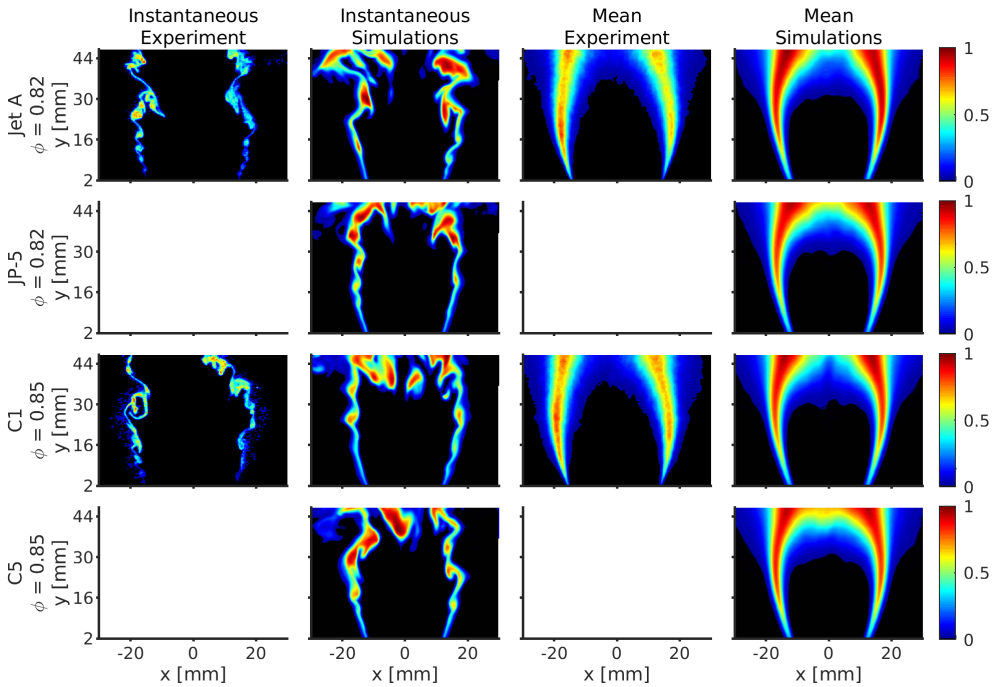

Figure 7.3: CH_2O distributions. Left to right: instantaneous CH_2O-PLIF results, instantaneous simulated number density, time-averaged CH_2O-PLIF results, time-averaged simulated number density. Top to bottom: Jet A, JP-5, C1, C5. Experimental data obtained from Pathania *et al.*, [7].

Figure 7.4 has the same structure as Fig. 7.3 but shows OH instead of CH_2O. OH is an indicator of the postflame and fully combusted zones. The overall shape of the OH distribution is reproduced quite well by the simulations, with some notable differences.

The OH-PLIF images suggest that the OH concentration should peak next to the inner reaction zone, with lower concentrations distributed throughout the RZ. Although the OH concentration is relatively high next to the inner reaction zone in the simulations as well, its peak is near the centerline at $y \sim 32$ mm. This difference between the experiments and simulations may have several causes. Firstly, although OH-PLIF measurements are correlated with actual number density, they are not necessarily proportional to it and should not be expected to match up perfectly with any simulation results. Secondly, all local reaction rates in the LES are assumed to be associated with the chemical time scale ν/s_u^2, which is logical in the preheat layer and inner reaction zone but less so in the postflame zone, where the chemical state changes more slowly. As a result, the conversion from OH to H_2O may be scaled down too strongly by the PaSR model, leading to broad OH-rich regions filling the RZ. The OH distributions predicted by the Z79 mechanisms (not shown) are more homogeneous than those predicted by the HyChem mechanisms; the homogeneity is correlated with the OH layer thickness in laminar flame simulations, which is consistently larger for Z79.

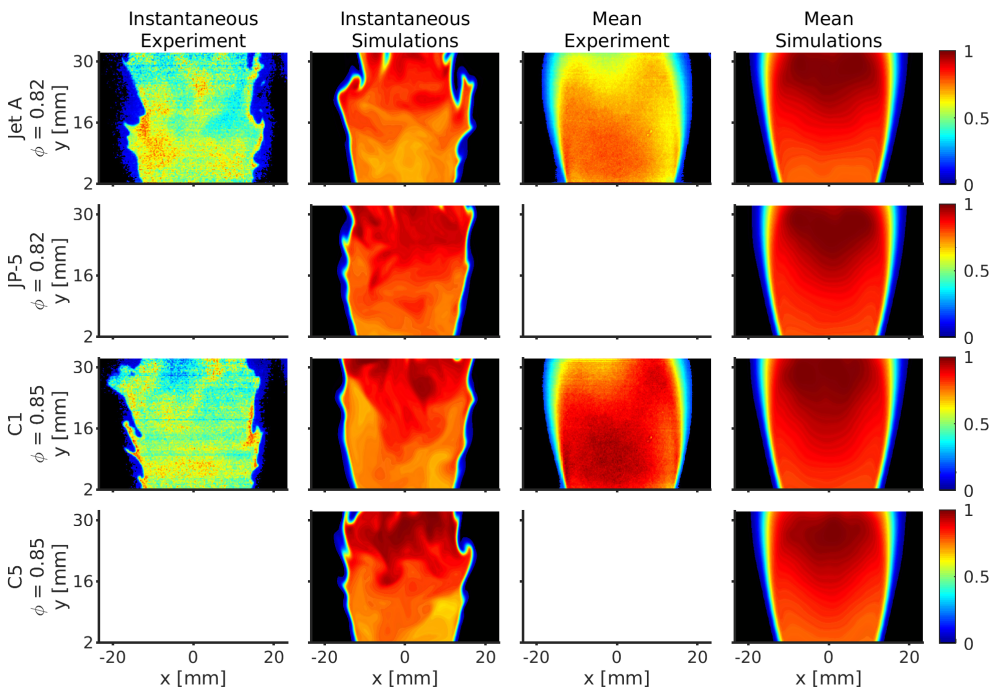

Figure 7.4: OH distributions. Left to right: instantaneous OH-PLIF results, instantaneous simulated number density, time-averaged OH-PLIF results, time-averaged simulated number density. Top to bottom: Jet A, JP-5, C1, C5. Experimental data obtained from Pathania *et al.*, [7].

Figure 7.5 quantifies the differences between the fuels in case A. Figure 7.5(a) shows $\langle D_f \rangle$ along the streamwise direction, with black symbols indicating $\langle D_f \rangle$ inferred from the experimental measurements on the Jet A flame. (The C1 measurements are within 1 mm of Jet A and therefore omitted.) At $y = 32$ mm, this is done by measuring the distance between the $\langle c \rangle = 0.5$ contours on opposite sides of the RZ, which is equivalent to $\langle D_f \rangle$. Since $\langle c \rangle$ is not available at $y = 45$ mm, a less certain estimate is required there: the distance between the peaks of the measured CH_2O distribution. With this uncertainty in mind, the simulations agree with the experiments in terms of $\langle D_f \rangle$. C1 has the largest flame. Jet A is relatively narrow until its inflection point, after which it merges with C1. JP-5 and C5 reach their inflection points first, after which they have the narrowest flames.

As seen in the OH distributions in Fig. 7.4, the turbulence in the shear layer stretches and deforms the flame sheet. These fluctuations are quantified using the standard deviation of D_f in Fig. 7.5(b). There is a clear fuel trend associated with the fluctuations: Jet A experiences the strongest fluctuations and C1 the weakest, with JP-5 and C5 forming a middle ground. This trend is most noticeable below the flame sheet inflection point. The stability of C1 may be partly attributed to its high LHV and ϕ, which increase HRR in the shear layer and thereby dilatation. This explanation is unsatisfactory, however, because it implies that C5 should have the weakest fluctuations and JP-5 the strongest, which is not the case. Interestingly, the strength of the fluctuations is correlated with CN, as shown in Fig. 7.5(c) using the normalized flame length. The flame length is computed from binarized snapshots of the OH concentration (like D_f) and represents the length of the curved flame front, averaged over time and across both sides of the bluff body, divided by the length of a perfectly stable and vertical flame. Only points below $y = 25$ mm are used. A longer flame length corresponds to greater deformation by turbulent fluctuations. Heptane is included alongside the jet fuels and follows the same trend. CN is an indicator of ignition quality, suggesting that ignition properties play a role in determining flame stability. This is surprising for a bluff body flame at atmospheric pressure, where combustion is driven by the turbulent diffusion of hot gases and the fuel mixture is $\sim$100 K below autoignition temperature. I propose the following mechanism to explain the connection.

When the flame sheet fluctuates outward, it bends convexly into the fuel-air mixture and triggers the thermal decomposition of the fuel around it. If the decomposition products that result from this are slow to react relative to the propagation speed of the flame, the reaction zone stops propagating outward and instead recedes toward its mean position. Low reactivity in the fuel decomposition products thus has a dampening effect on fluctuations. To quantify this, we introduce the ratio $\tau_{ign,d}/\tau_u$, where $\tau_{ign,d}$ is the ignition delay time of the fuel decomposition products and τ_u is the time scale of flame propagation, defined as $\tau_u = \delta_u/s_u$. How $\tau_{ign,d}$ is best computed is not a trivial question, but here it is defined as τ_{ign} for a characteristic mixture of small hydrocarbons obtained for each fuel from ignition simulations. (For more details, see paper I.) If $\tau_{ign,d}/\tau_u \ll 1$, the decomposition products

react quickly relative to flame propagation, and there is no dampening. If $\tau_{ign,d}/\tau_u \sim 1$ or $\tau_{ign,d} \gg 1$, the low reactivity affects time scales similar to or longer than that of flame propagation, and fluctuations may be dampened. The ratio $\tau_{ign,d}/\tau_u$ is plotted in Fig. 7.5(d) against the temperature-based flame progress variable $(T - T_u)/(T_b - T_u)$, where T_b is obtained from laminar flame simulations. For most temperatures, C1 experiences the slowest ignition of its decomposition products and Jet A the fastest, with JP-5 and C5 forming a middle ground - the same trend as for the fluctuation intensity.

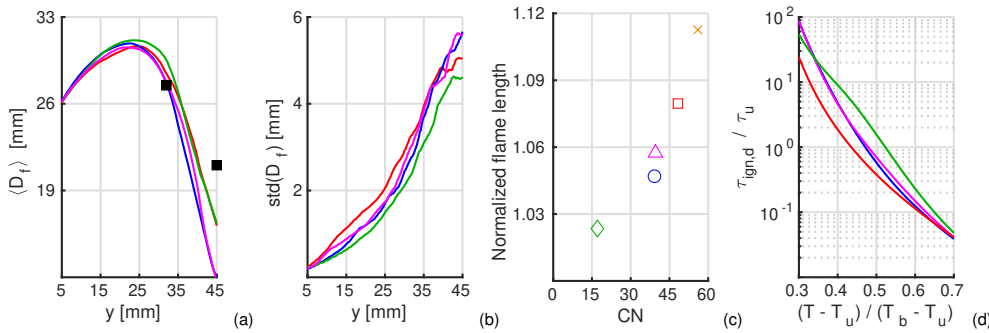

Figure 7.5: Mean flame sheet diameter (a), standard deviation of flame sheet diameter (b), normalized flame length versus CN (c), and $\tau_{ign,d}/\tau_u$ versus temperature-based flame progress variable (d). Legend: Jet A (red), JP-5 (blue), C1 (green), C5 (magenta), n-heptane (orange), estimated D_f from Pathania *et al.*, [7], (black).

As shown in Fig. 7.5, different $\langle D_f \rangle$ are predicted for the different fuels. To investigate the underlying cause of the trend, in Fig. 7.6, $\langle D_f \rangle$ is plotted against several other parameters: the RZ length L_R, the temperature ratio TR_{RZ} based on the RZ temperature, the laminar temperature ratio TR_L, the laminar flame speed s_u, and the turbulent Damköhler number $\mathrm{Da_T}$. The top row shows the maximum $\langle D_f \rangle$, which is equivalent to $\langle D_f \rangle$ at the inflection point of the mean flame sheet. The bottom row shows $\langle D_f \rangle$ at $y = 45$ mm, near the end of the RZ. Several sets of simulations are included: the HyChem simulations (red), the Z79 simulations (blue), and the Z79 simulations with the same base chemistry block as Jet A (yellow). There is no yellow symbol for Jet A, as it would be identical to the blue symbol. $\langle D_f \rangle$ is correlated with L_R, which is logical as a larger flame is recirculated further downstream compared to a smaller flame. $\langle D_f \rangle$ is also correlated with TR_{RZ}, at least at the inflection point, confirming that the flames adhere to the scaling law proposed by Massey *et al.*, [75], which states that L_R increases with TR. There is no clear correlation between $\langle D_f \rangle$ and TR_L, however, suggesting that TR_L cannot be reliably used to predict TR_{RZ}. Likewise, $\langle D_f \rangle$ does not visibly correlate with either s_u or $\mathrm{Da_T}$; both of these parameters should theoretically increase resistance to recirculation, but the results suggest that this connection is either insignificant or incorrectly reproduced by the simulations.

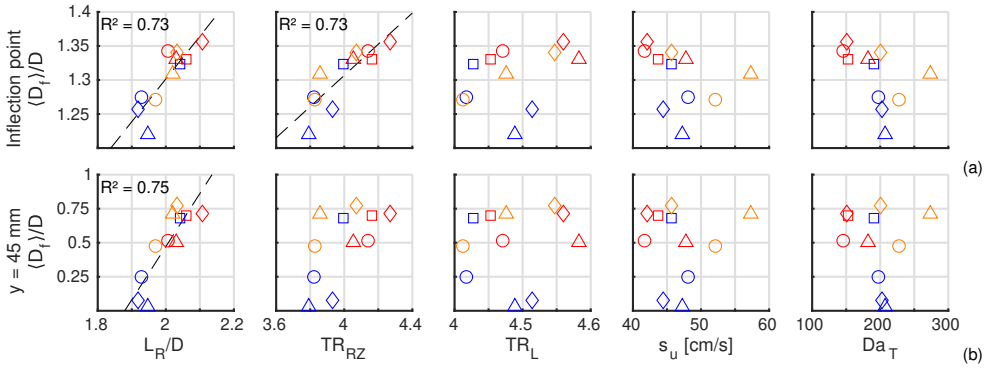

Figure 7.6: Mean flame diameter at the inflection point (a) and at y = 45 mm (b), plotted against L_R, TR_{RZ}, TR_L, s_u, and Da_T. Color legend: HyChem (red), Z79 (blue), Z79 with base chemistry of Jet A (yellow). Symbol legend: Jet A (squares), JP-5 (circles), C1 (diamonds), C5 (triangles).

7.4 Spray flame characteristics

The following sections discuss results from case B. Figure 7.7 shows the distribution of liquid fuel (a), HRR (b), and OH mass fraction (c) at idle conditions. The data is averaged over time and along the azimuthal direction, and all panels are normalized separately. Experimental data from Meier *et al.*, [8], consisting of kerosene-PLIF, OH chemiluminescence, and OH-PLIF are included for comparison. Again, note that although PLIF is useful for visualizing the fuel and OH concentrations, the PLIF signal is not necessarily proportional to the local concentration of the targeted species. Similarly, OH chemiluminescence indicates regions of high chemical activity but does not directly correspond to HRR. For these reasons, the simulation results should not be expected to match the experimental data perfectly. With this limitation in mind, the spray and flame structure is reproduced well by the simulations. The largest discrepancy is visible in the HRR and OH distributions, which are slightly too lifted; their centers are located too far away from the fuel injection point. The results are qualitatively similar for all fuels, although the spray penetration depth is slightly larger for Jet A.

Figure 7.8 has the same structure as Fig. 7.7 but contains results at cruise conditions instead. All panels are normalized separately. The simulated spray and flame structure for Jet A is well within the expected uncertainty when compared to the experiments. The spray and flame are more compact than at idle conditions, and the path from unburnt fuel to complete combustion products is considerably shorter. The fuels are also more distinct; the sprays and flames of C1 and C5 are more compact compared to Jet A, and the OH distribution is relatively high downstream of the C1 flame.

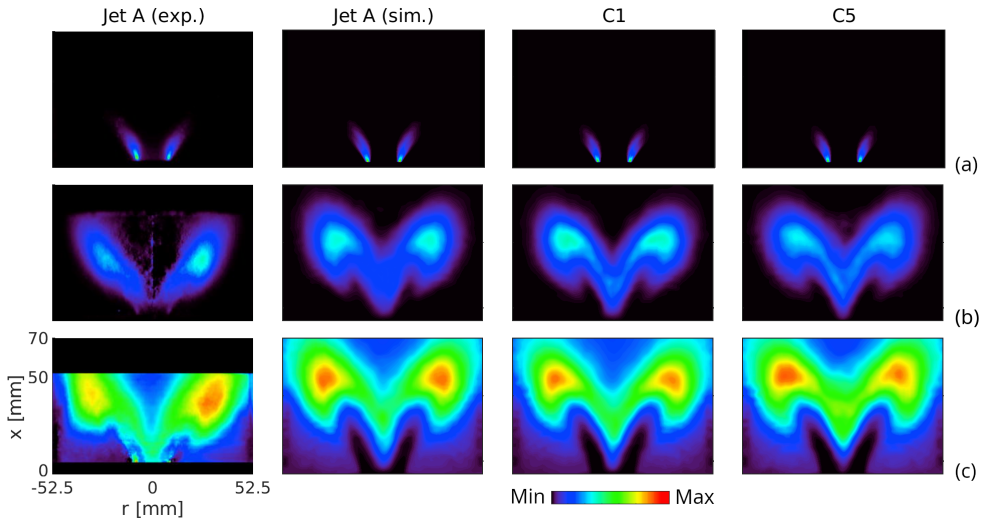

Figure 7.7: Time-averaged, azimuthally integrated liquid concentration (a), HRR (b), and OH mass fraction (c) at idle conditions. Experimental kerosene-PLIF, OH chemiluminescence, and OH-PLIF measurements obtained from Meier *et al.*, [8], are included in the leftmost column for comparison.

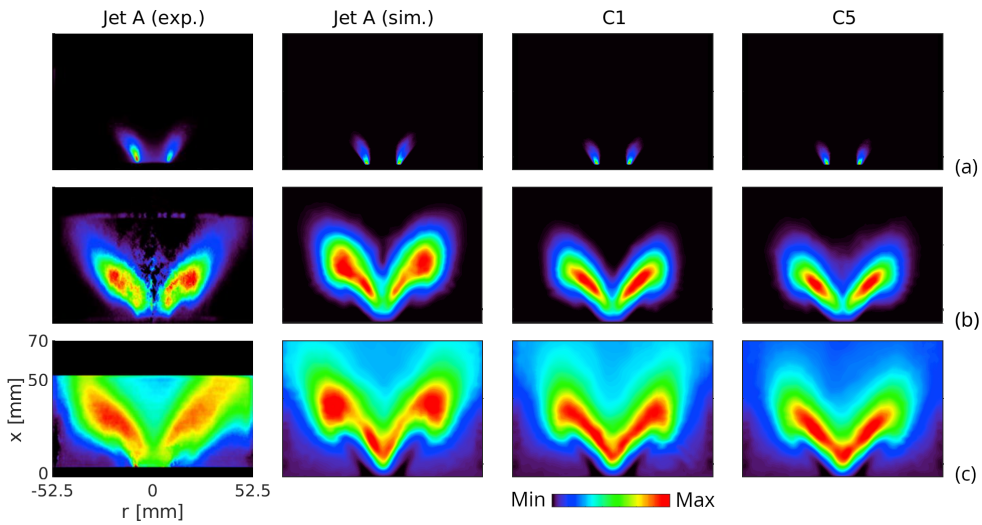

Figure 7.8: Time-averaged, azimuthally integrated liquid concentration (a), HRR (b), and OH mass fraction (c) at cruise conditions. Experimental kerosene-PLIF, OH chemiluminescence, and OH-PLIF measurements obtained from Meier *et al.*, [8], are included in the leftmost column for comparison.

Figure 7.9 shows some key statistics extracted from the spray at idle (a) and cruise (b) conditions. These include SMD, axial velocity, and droplet temperature along the radial direction at three distances from the prefilmer lip: $x = 10$ mm, $x = 15$ mm, and $x = 20$

mm. It should be noted that the reliability of the data is relatively low at $y = 20$ mm, as only a small fraction of droplets remain at that point. All simulation results are temporally and azimuthally averaged. Experimental measurements of SMD and axial velocity (only available at idle conditions) from Meier *et al.*, [8], are included for comparison. The vaporization progress, defined as the reduction in liquid mass flux since injection, is given as percentages. The simulation results for Jet A show adequate agreement with the experimental data near the injection point but diverge further downstream. The main points of divergence lie in the width of the velocity distribution and the diameter of the outermost droplets, which are both underpredicted. Both of these discrepancies likely stem from an overprediction of the temperature in the ORZ, a consequence of assuming adiabatic walls. A lower ORZ temperature would have resulted in a greater density gradient between the CRZ and ORZ, likely making the CRZ wider. The inner shear layer, which stabilizes the flame, and the main flow cone, which transports the spray, would thus also become wider.

All fuels have virtually identical droplet velocity distributions, demonstrating that the path taken by the droplets is independent of their thermodynamic properties. Their SMD and temperature profiles differ, however. C1 has smaller droplets than Jet A due to its lower σ and ρ, and it also experiences faster vaporization due to its higher volatility. C5 has low σ, low μ, low ρ, and the highest volatility, which together result in C5 having the smallest droplets. The different distillation curves of the fuels are evident in the temperature profiles; the higher the average boiling point of each fuel, the higher its mean spray temperature. The spray penetration depth follows the volatility trend: C5 evaporates the fastest and has the shortest spray, followed by C1, then Jet A.

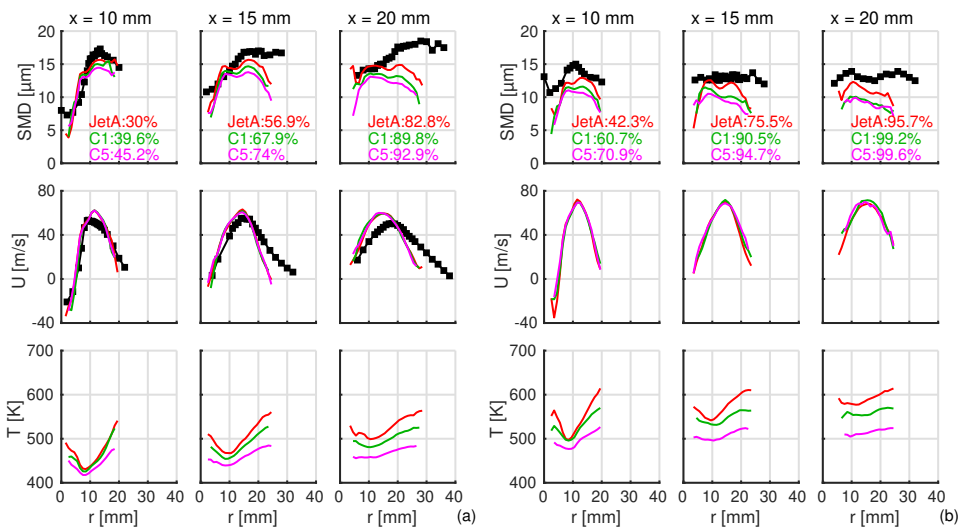

Figure 7.9: Spray statistics at idle (a) and cruise (b) conditions, at three distances from the burner. Top to bottom: SMD, axial velocity, temperature. Percentages refer to vaporization progress. Legend: Jet A (red), C1 (green), C5 (magenta), experimental data obtained from Meier *et al.*, [8], for Jet A (black).

Figure 7.10 visualizes the combustion process by showing the temporally and radially averaged density of four key intermediate species along the streamwise direction: the fuel species, C_2H_4, i-C_4H_8, and OH. The fuel species is $C_{11}H_{22}$, $C_{13}H_{28}$, and $C_{10}H_{19}$ for Jet A, C1, and C5, respectively. At idle conditions, Fig. 7.10(a), all fuels are vaporized similarly but differ greatly in their subsequent thermal decomposition. C5 contains the most aromatics, and its decomposition consequently results in a high amount of C_2H_4. C1 consists solely of iso-paraffins, which means that it is considerably less likely to decompose into C_2H_4. C1 stands out by forming much more i-C_4H_8, a heavier and more stable species. All fuels produce very similar OH distributions, as demonstrated previously.

At cruise conditions, Fig. 7.10(b), the gaseous fuel distribution is affected by flame lift as the vaporized Jet A occupies a larger region compared to the other fuels. As a consequence, the C_2H_4 peaks of Jet A and C5 become quite similar; C5 forms more C_2H_4, but it is consumed more quickly and occupies a smaller region. Jet A and C5 have similar OH distributions at $x = 100$ mm, but the C1 flame produces considerably more OH. This is a result of the different chemical pathways taken by i-C_4H_8 during combustion, which at the high temperatures and pressures of cruise conditions produce a higher product temperature and more OH.

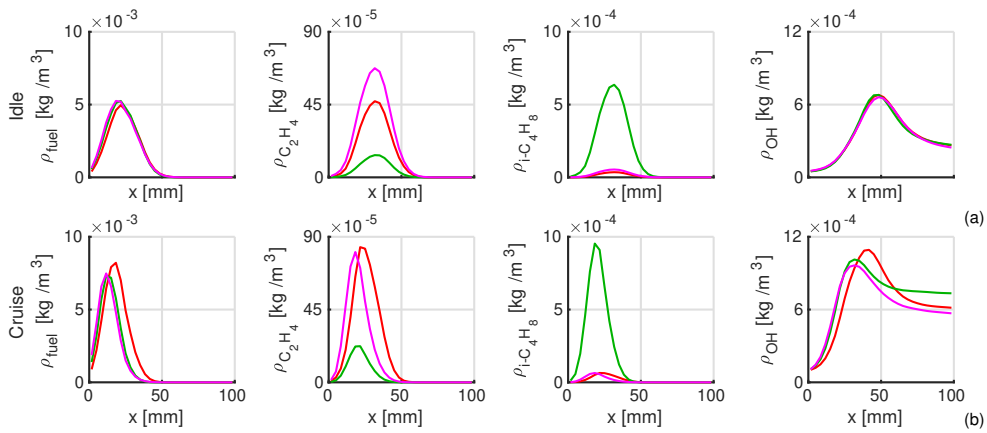

Figure 7.10: Radially averaged density of important gaseous species plotted along the streamwise direction at idle (a) and cruise (b) conditions. Legend: Jet A (red), C1 (green), C5 (magenta).

7.5 Emissions

The HyChem chemical reaction mechanisms are detailed enough to capture how the different compositions of the fuels lead to different processes of thermal decomposition, oxidation, and emission generation (for major species). The major emission species considered here are CO_2, H_2O, CO, OH, and NO_x. To obtain accurate results for other emissions,

such as unburnt hydrocarbons and soot, more detailed mechanisms are required. For this reason, the analysis is limited to the major species and focus on how these are affected by composition, liquid properties, and flame shape. As explained in the previous chapter, NO_x formation is not modeled directly in the simulations but calculated by post-processing the simulation results. As also explained in the previous chapter, the lean flame and lack of quenching/dilution jets in case B results in relatively low CO and high OH emissions compared to typical jet engines.

Table 7.1 shows Emission Indices (EI) for the major species in each simulation. The CO_2 and H_2O emissions are essentially determined by the H/C ratio of each fuel. CO and OH are heavily influenced by the temperature in the emissions, which in turn is determined by the LHV and global ϕ of each fuel, which also ultimately stem from the H/C ratio. In the HyChem mechanisms, C1 has the highest LHV, ϕ, EICO, and EIOH, whereas C5 is on the other end of the spectrum. Unlike CO and OH, which mainly depend on the emission temperature, NO_x is heavily dependent on the local flame temperature. NO_x is therefore the most sensitive to the flame shape; the local z is particularly important as it determines the local temperature. Figure 7.11 shows PDFs of HRR versus z at idle (a) and cruise (b) conditions in each simulation. The means and standard deviations of the distributions are also given, and z is normalized by its stoichiometric value z_{st}, which is slightly different for each fuel. The dashed lines represent $EINO_x$ as a function of z for each fuel, as predicted by laminar flame simulations. As described in the previous chapter, the integrated product of the HRR PDF and the $EINO_x$ function yields the final $EINO_x$ value; the more the two curves overlap, the higher $EINO_x$ will be.

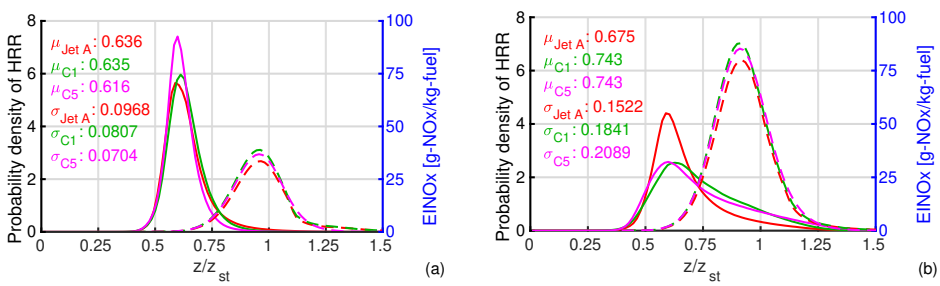

Figure 7.11: Probability distributions of HRR versus z/z_{st} (solid lines), and $EINO_x$ as a function of z/z_{st} (dashed lines) at idle (a) and cruise (b) conditions. Means and standard deviations of HRR are denoted μ_{fuel} and σ_{fuel}. Legend: Jet A (red), C1 (green), C5 (magenta).

Figure 7.11(a) shows that at idle conditions, the HRR is concentrated around $z/z_{st} \sim 0.6$, which approximately corresponds to the global FAR (excluding cooling air). This implies a high degree of premixing between the air and fuel, which is logical considering the relatively high flame lift at idle conditions. In other words, the flame is partially premixed but has a mostly premixed character. Since the flame mostly occupies the same position regardless

of fuel, as shown in Fig. 7.7, the rapid vaporization of C5 provides more time for the gaseous fuel to mix with the air, lowering z and giving it a sharper peak. The same is true for C1, but the effect is compensated for by the relatively high global ϕ of C1, giving Jet A and C1 strikingly similar PDFs at idle conditions. Jet A and C1 consequently have almost equal $EINO_x$, whereas it is ∼40% lower for C5. The picture changes at cruise conditions, Fig. 7.11(b), where all fuels have much wider distributions. This is because the flame lift is considerably shorter, giving the fuel less time to mix with the air, thus making the flame less premixed. C1 and C5 have particularly wide distributions, with a significant portion of reactions taking place under fuel-rich conditions. However, the means of the distributions are still close to the global FAR. Since the separation between the spray and flame is quite short at cruise conditions, the vaporization rate has a strong effect on the flame lift. If the vaporization rate is fast, there is less mixing and the HRR distribution is shifted towards z_{st}, which increases $EINO_x$. This is why C1 and C5 have the highest $EINO_x$ at cruise conditions and Jet A the lowest. As the most volatile fuel, C5 has the most compact flame and experiences the most fuel-rich combustion. However, the higher LHV and ϕ of C1 compensate for this, ultimately giving C1 a slightly higher $EINO_x$. Raising the fuel flow rate of C5 to match the power (or thrust) of the C1 simulation would give it the highest $EINO_x$ of the fuels.

Table 7.1: Emission indices of CO, CO_2, OH, H_2O, and NO_x, given in grams of emissions per kilogram of burnt fuel.

	Idle			Cruise		
	Jet A ϕ: 0.735	C1 ϕ: 0.745	C5 ϕ: 0.728	Jet A ϕ: 0.714	C1 ϕ: 0.724	C5 ϕ: 0.707
$EICO_2$	3140	3110	3160	3150	3110	3160
EIH_2O	1280	1370	1230	1280	1370	1230
EICO	1.1	1.2	0.9	1.3	1.7	1.0
EIOH	7.7	8.4	6.8	8.9	10.5	7.8
$EINO_x$	2.4	2.3	1.4	15	27	24

7.6 Thermoacoustics

When the pressure rises near the flame in case B, the HRR rises in response, forming a thermoacoustic feedback loop. Two types of thermoacoustic oscillations are present in the simulations of case B: a longitudinal oscillation with a frequency of ∼1.6 kHz and an azimuthal oscillation with a frequency of ∼4.2 kHz. Figure 7.12(a) visualizes these two modes as spatial functions ranging from -1 to 1, extracted from the simulation results using proper orthogonal decomposition of the pressure field, [76]. The top image shows the (first) longitudinal acoustic mode, which belongs to a pressure wave traveling back and forth

between the swirlers and the exit. The bottom image shows the (first) azimuthal acoustic mode, which belongs to a pressure wave traveling around the central x axis. The normalized coefficients of these two modes are shown over time in Fig. 7.12(b). Multiplying the time-dependent coefficient with the corresponding spatial function produces a simplified reconstruction of the actual pressure oscillation observed in the simulation.

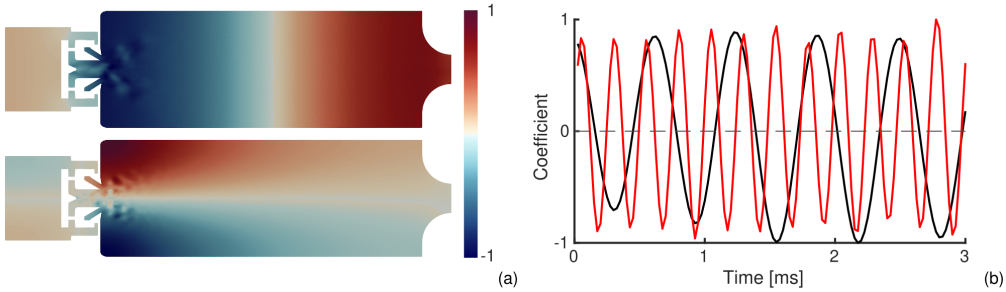

Figure 7.12: Excited longitudinal (top) and azimuthal (bottom) acoustic modes (a), alongside the corresponding longitudinal (black) and azimuthal (red) time-dependent coefficients (b).

The azimuthal oscillations give rise to a constant azimuthal asymmetry in the HRR, but do not affect the total integrated HRR or the amount of liquid fuel in the combustor. They are also significantly weaker than the longitudinal oscillations in terms of pressure amplitude. The longitudinal oscillations, on the other hand, can give rise to HRR peaks throughout the flame accompanied by a temporary increase in the spray vaporization rate. To visualize this, figure 7.13 shows the fluctuations of the total liquid mass m_{liq} and near-flame pressure p in each simulation over 10 ms at idle (a) and cruise (b) conditions. Both are given as percentages of the mean values $\langle m_{liq} \rangle$ and $\langle p \rangle$. At idle conditions, both the liquid mass and the pressure do experience oscillations, but the periodicity is very subtle. The amplitude of the longitudinal pressure oscillations are on average $\sim$0.2% of the mean combustor pressure, or around 1 kPa. The effect is small compared to the unsteadiness caused by turbulence, and the fuels are not significantly different from each other. The picture is quite different at cruise conditions, where C1 and C5 experience very distinct longitudinal oscillations, whereas Jet A remains at $\sim$0.2%. For C1 and C5, the pressure peaks are typically associated with a rapid decrease in liquid mass, indicating an accelerated vaporization rate and a shortening of the spray. When the pressure subsequently drops, the spray grows and the liquid mass peaks. The average pressure amplitude is 0.97% for C1 and 1.31% for C5, but a longer sampling period would be required to determine whether the difference between these two fuels is statistically significant, as the amplitude is subject to low-frequency ($<$100 Hz) changes over time.

The strong thermoacoustic oscillations of C1 and C5 have a significant impact on the flame dynamics. As shown previously in Fig. 7.11, C1 and C5 burn over a wider range of z compared to Jet A. This is partly due to their short flame lift, which gives their flames non-

premixed characteristics, but also due to the thermoacoustic variation of the spray length. When the HRR peaks and the spray becomes short, the reaction zone moves relatively close to the spray and high z, which increases the average NO_x concentration in the emissions. The oscillatory nature of the C1 and C5 flames should also make them more prone to blowout, but the fuel mass flow would have to be reduced to test this hypothesis.

Why do C1 and C5 experience stronger thermoacoustic oscillations than Jet A? The trend appears correlated with volatility, suggesting that the vaporization rate more easily couples to pressure oscillations for volatile fuels. The vapor pressure scales exponentially with droplet temperature, which means that the local temperature peaks associated with the HRR peaks have a stronger effect on C5 than, e.g., Jet A. CN may also play a role, as suggested by Bae *et al.*, [77]. The time scales associated with the longitudinal pressure oscillations are on the order of 0.1 ms, and as Fig. 3.5 shows, τ_{ign} is inversely proportional to CN at these time scales (in the HyChem model). The relatively fast ignition of Jet A may dampen incipient thermoacoustic oscillations, as the HRR stays relatively high even after a pressure-induced peak.

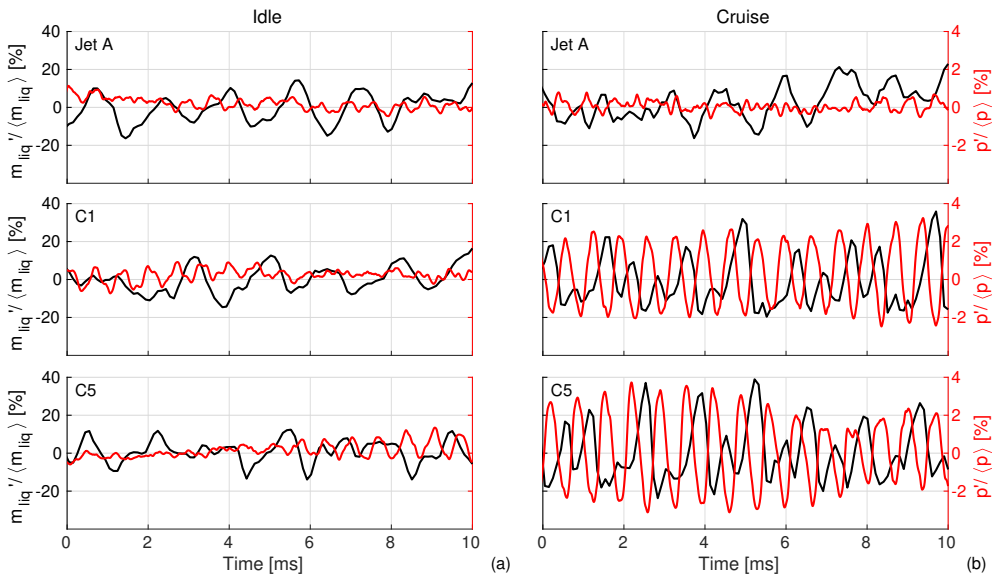

Figure 7.13: Normalized liquid mass fluctuation (black) and normalized pressure fluctuation (red) over time at idle (a) and cruise (b) conditions. Top to bottom: Jet A, C1, C5.

Chapter 8

Concluding remarks

This work uses LES to explore how the composition and fundamental characteristics of jet fuels affect their turbulent combustion behavior. The following is a summary of the findings and a list of suggestions for future work.

8.1 Validation and model sensitivity

The simulation methodology is capable of accurately reproducing experimental observations in premixed flames (case A) and spray flames (case B). The mesh sensitivity is considerable in both cases, but $\sim$2 cells over the laminar flame width was identified as a critical resolution threshold for case A. The choice of turbulence-chemistry interaction model also has a substantial effect on the results; the PaSR model is found to produce good results here, but I recommend that several models be tested during the design phase of future studies. The choice of chemical reaction mechanism can also impact the size and behavior of the flame, as shown by the differences between the predictions of the HyChem and Z79 families of reaction mechanisms. The difference can be predicted *a priori* by comparing the flame temperature in laminar flame simulations using the different mechanisms.

8.2 Fuel comparison

This work focuses on Jet A, C1, and C5. These fuels have radically different compositions and thermochemical properties, but the properties with the largest direct impact on the results are vaporizability, CN, and H/C. Vaporizability refers to the tendency of the fuel to be vaporized and is affected by atomizability and volatility. Atomizability is affected

by viscosity, density, and surface tension, but volatility appears to be the dominant factor for the vaporization rate. Volatility is determined by the distillation curve. CN describes ignition quality and is approximately inversely proportional to τ_{ign}. H/C is determined by the amount of cyclic hydrocarbons in the fuel, such as aromatics; a high fraction of cyclic compounds results in a low H/C and vice versa. Table 8.1 summarizes the fuel trends observed in the present work and states which fundamental or emergent fuel parameter they are most influenced by. Vaporizability, CN, and H/C are included for comparison. The labels "High", "Medium", and "Low" are only used to compare the fuels among themselves and are not based on any external criterion or judgment of their quality as fuels.

In case A, the diameter of the flame sheet is strongly correlated with the length of the RZ. Both of these parameters can thus be used to quantify the overall flame size. The flame size is correlated with the flame temperature. It would be logical for the turbulent flame temperature to be strongly correlated with the corresponding laminar flame temperature, but this is not demonstrated by the simulations. If only a single fuel is considered, however, the laminar flame temperature can reliably be used to predict the relative flame sizes produced by two different chemical reaction mechanisms. This suggests that other fuel parameters influence the turbulent flame temperature, but these remain unidentified. When all fuels studied in this work are considered, there is no significant statistical relation between flame size and s_u, $\mathrm{Da_T}$, or K_{ext}.

The mean magnitude of turbulent fluctuations in the flame sheet in case A appears to be correlated with CN, suggesting a connection to ignition quality. I propose that the key property to consider is the ratio between τ_{ign} of the thermally decomposed fuel and the time scale of flame propagation, which is determined by s_u and δ_u. If the decomposed fuel is slow to react, outward fluctuations in the flame sheet may be dampened.

In case B, all results are influenced by H/C since it affects ϕ when the fuel mass flow is constant. Vaporizability visibly reduces the spray length, droplet size, and droplet temperature. The average droplet temperature trend is determined by the volatility trend. The droplet velocity, on the other hand, appears to be independent of fuel properties. At idle conditions, where the pressure and preheat temperature are low, all fuels have similar flame shapes and flame lifts. This occurs because the separation between the spray and flame is large regardless of fuel, which allows the vaporized fuel to be relatively thoroughly mixed with the surrounding air. C5 has the shortest spray and thus the highest degree of premixing, which (in addition to its low H/C) gives it the lowest EINO_x. The situation is different at cruise conditions, where the spray-flame separation is low and the flame is less premixed; the vaporizability then plays a greater role, and C1 and C5 have significantly lower flame lifts compared to Jet A. The lower flame lift results in more reactions near stoichiometric conditions, increasing the local temperature and thereby EINO_x. C1 and C5 are also found to experience significantly stronger thermoacoustic oscillations than Jet A; this may be a result of their lower CN, which slows down the regression to the mean

after a temporary heat release peak, or their higher vaporizability, which allows for greater fluctuations in the vaporization rate.

Table 8.1: Summary of known and observed fuel trends, and the parameters these trends are mainly influenced by. The labels "High" (red), "Medium" (yellow), and "Low" (blue) are only used to compare the fuels among themselves and are not based on any external criterion or judgment of their quality as fuels.

Parameter	Jet A	C1	C5	Influenced by
Vaporizability	Low	Medium	High	Composition
CN	48.3	17.1	39.6	Ignition
Modeled H/C	2	2.15	1.9	Composition
Premixed flame size	High	High	Low	Flame temperature[a]
Premixed fluctuations	High	Low	Medium	CN
Spray length	High	Medium	Low	Vaporizability
Droplet size	High	Medium	Low	Vaporizability
Droplet velocity	Medium	Medium	Medium	Independent
Droplet temperature	High	Medium	Low	Vaporizability
Flame lift (idle)	Medium	Medium	Medium	Strong premixing
Flame lift (cruise)	High	Low	Low	Vaporizability
EINO$_x$ [g/kg] (idle)	2.4	2.3	1.4	Spray length, H/C
EINO$_x$ [g/kg] (cruise)	15	27	24	Flame lift, H/C
Thermoacoustics	Low	High	High	CN/Vaporizability[b]

[a] Refers to the temperature in the actual flame, which does not clearly correlate with adiabatic flame temperature across fuels. The adiabatic flame temperature can be used to predict flame size when comparing different chemical reaction mechanisms for a single fuel, however.

[b] The potential connections to vaporizability and CN are speculative and require further research.

8.3 Open questions

This work identifies many fuel trends, but many of them remain hypothetical until more data is gathered. Others are still unexplained. The following is a list of inquiries I would like to see explored in future work:

- The premixed bluff body flames in case A appear to have a critical mesh resolution threshold located somewhere between two and three cells per laminar flame thickness. Where is this threshold located more exactly? Can it be explained?
- The flame temperature in case A is different for each fuel, but the trend differs from that of the adiabatic flame temperature. Why? Does this occur in reality?
- In case A, the mechanism proposed to explain why some fuels experience stronger or weaker fluctuations in the flame sheet should be investigated further. Does it

hold when more fuels and operating conditions are considered? Can the mechanism itself, or a more accurate alternative, be observed directly? Can the ratio between the time scales of decomposed ignition and flame propagation be used to quantify it? Note that the mechanism is only proposed for non-oxygenated hydrocarbon fuels that undergo thermal decomposition, but it could theoretically apply to a broader category of fuels.

- Since vaporizability has a large impact on the behavior of spray flames (case B), can the liquid thermodynamics model be made more realistic? Can the shape of the distillation curve be incorporated?
- What happens when the fuel is modeled as a surrogate mix of a few key species rather than a single lumped species?
- Can the propensity of a fuel to generate thermoacoustic oscillations be predicted using its CN, vaporizability, or some other property?

8.4 Final thoughts

This work represents a minor contribution to our understanding of alternative jet fuel combustion. With further numerical, experimental, and industrial research, I am confident that we will eventually become as proficient in using and understanding bio-derived fuels as we are with conventional fossil fuels. I hope that one day, using sustainable fuels will be so natural and obvious that this thesis will seem like an irrelevant relic from a more uncertain, kerosene-propelled era.

References

[1] H. Ritchie. What share of global CO2 emissions come from aviation? *Our World in Data*, 2024. Available at: https://ourworldindata.org/global-aviation-emissions (Accessed: 29th February 2024).

[2] Net-Zero Carbon Emissions by 2050. *IATA*, 2021. Available at: https://www.iata.org/en/pressroom/pressroom-archive/2021-releases/2021-10-04-03/ (Accessed: 29th February 2024).

[3] Conversion processes. *ICAO*, 2024. Available at: https://www.icao.int/environmental-protection/GFAAF/Pages/Conversion-processes.aspx (Accessed 7 August 2024).

[4] ASTM International. D7566 Standard Specification for Aviation Turbine Fuels Containing Synthesized Hydrocarbons, 2024.

[5] SAF Volumes Growing but Still Missing Opportunities. *ICAO*, 2023. Available at: https://www.iata.org/en/pressroom/2023-releases/2023-12-06-02 (Accessed 7 August 2024).

[6] C. Fureby. Large eddy simulation modelling of combustion for propulsion applications. *Phil. Trans. R. Soc. A*, 367:2957–2969, 2009.

[7] R.S. Pathania, A.W. Skiba, and E. Mastorakos. Experimental investigation of unconfined turbulent premixed bluff-body stabilized flames operated with vapourised liquid fuels. *Combust. Flame*, 227:428–442, 2021.

[8] U. Meier, J. Heinze, S. Freitag, and C. Hassa. Spray and Flame Structure of a Generic Injector at Aero-engine Conditions. *J. Eng. Gas Turbines Power*, 134:031503, 2012.

[9] A.E.S.E.T. Alajmi, N.M. Adam, A.A. Hairuddin, and L.C. Abdullah. Fuel atomization in gas turbines: A review of novel technology. *Int. J. Energy Res.*, 43:3166–3181, 2019.

[10] D.S. Lee, D.W. Fahey, P.M. Forster, P.J. Newton, R.C. N Wit, L.L. Lim, B. Owen, and R. Sausen. Aviation and global climate change in the 21st century. *Atmos. Environ.*, 43:3520–3537, 2009.

[11] P. Flohr and P. Stuttaford. Combustors in gas turbine systems. In P. Jansohn, editor, *Modern Gas Turbine Systems*, Woodhead Publishing Series in Energy, pages 151–191. Woodhead Publishing, Cambridge, 2013.

[12] S. Samuelsen. Rich burn, Quick-mix, Lean burn (RQL) combustor. In *The gas turbine handbook*, pages 227–233. US Department of Energy, Office of Fossil Energy, National Energy Technology Laboratory, Morgantown, 2006.

[13] T. Poinsot. Prediction and control of combustion instabilities in real engines. *Proc. Combust. Inst.*, 36:1–28, 2017.

[14] B.T. Paxton, C.A. Fugger, A.S. Tomlin, and A.W. Caswell. Experimental Investigation of Fuel Chemistry on Combustion Instabilities in a Premixed Bluff-Body Combustor. In *Proceedings of the AIAA Scitech 2020 Forum*, Orlando, 6–10 January, 2020. AIAA 2020-0174.

[15] Kerosene. *U.S. Energy Information Administration*. Available at: https://www.eia.gov/tools/glossary/index.php?id=kerosene (Accessed 27 Mar 2025).

[16] Civil Jet Fuel. *Shell*. Available at: https://www.shell.com/business-customers/aviation/aviation-fuel/civil-jet-fuel-grades.html (Accessed 27 Mar 2025).

[17] ASTM International. D1655 Standard Specification for Aviation Turbine Fuels, 2024.

[18] T. Edwards. Reference Jet Fuels for Combustion Testing. In *Proceedings of the 55th AIAA Aerospace Sciences Meeting*, Grapevine, 9–13 January, 2017. AIAA 2017-0146.

[19] H. Ruan, Y. Qin, J. Heyne, R. Gieleciak, M. Feng, and B. Yang. Chemical compositions and properties of lignin-based jet fuel range hydrocarbons. *Fuel*, 256:115947, 2019.

[20] K. G. Joback and R. C. Reid. ESTIMATION OF PURE-COMPONENT PROPERTIES FROM GROUP-CONTRIBUTIONS. *Chem. Eng. Commun.*, 57:233–243, 1987.

[21] NIST Standard Reference Database Number 69. In P.J. Lindstrom and W.G. Mallard, editors, *NIST Chemistry WebBook*. National Institute of Standards and Technology. Available at: https://webbook.nist.gov/chemistry/ (Accessed 28 Mar 2025).

[22] SpringerMaterials. *Springer Nature*. Available at: https://materials.springer.com (Accessed 28 Mar 2025).

[23] J. Yanowitz, M.A. Ratcliff, R.L. McCormick, J.D. Taylor, and M.J. Murphy. Compendium of experimental cetane numbers. Technical report, National Renewable Energy Lab. (NREL), 2017. NREL/TP-5400-67585.

[24] D. Carpenter, S. Nates, F.L. Dryer, and S.H. Won. Evaluating ignition propensity of high cycloparaffinic content alternative jet fuel by a chemical functional group approach. *Combust. Flame*, 223:243–253, 2021.

[25] M. Colket, J. Heyne, M. Rumizen, M. Gupta, T. Edwards, M. Roquemore, G. Andac, R. Boehm, J. Lovett, R. Williams, J. Condevaux, D. Turner, N. Rizk, J. Tishkoff, C. Li, J. Moder, D. Friend, and V. Sankaran. Overview of the National Jet Fuels Combustion Program. *AIAA J.*, 55:1087–1104, 2017.

[26] R. Xu, K. Wang, S. Banerjee, S. Jiankun, T. Parise, Z. Yangye, W. Shengkai, A. Movaghar, L. Dong Joon, Z. Runhua, H. Xu, G. Yang, L. Tianfeng, K. Brezinsky, F.N. Egolfopoulos, D.F. Davidson, R.K. Hanson, C.T. Bowman, and H. Wang. A physics-based approach to modeling real-fuel combustion chemistry – II. Reaction kinetic models of jet and rocket fuels. *Combust. Flame*, 193:520–537, 2018.

[27] J. Yu and S. Eser. Determination of critical properties (Tc, Pc) of some jet fuels. *Ind. Eng. Chem. Res.*, 34:404–409, 1995.

[28] H. Wang, R. Xu, K. Wang, C.T. Bowman, R.K. Hanson, D.F. Davidson, K. Brezinsky, and F.N. Egolfopoulos. A physics-based approach to modeling real-fuel combustion chemistry - I. Evidence from experiments, and thermodynamic, chemical kinetic and statistical considerations. *Combust. Flame*, 193:502–519, 2018.

[29] E. Ranzi, A. Frassoldati, A. Stagni, M. Pelucchi, A. Cuoci, and T. Faravelli. Reduced Kinetic Schemes of Complex Reaction Systems: Fossil and Biomass-Derived Transportation Fuels. *Int. J. Chem. Kinet.*, 46:512–542, 2014.

[30] Ansys Chemkin-Pro, Ver. 2021 R2. *Ansys*, 2021.

[31] B.-J. Zhong, H.-S Peng, and D. Zheng. The effect of different class of hydrocarbons on laminar flame speeds of three C7 fuels. *Fuel*, 225:225–229, 2018.

[32] B. Franzelli, E. Riber, M. Sanjosé, and T. Poinsot. A two-step chemical scheme for kerosene–air premixed flames. *Combust. Flame*, 157:1364–1373, 2010.

[33] K. Wang, R. Xu, T Parise, J. Shao, A. Movaghar, D.J. Lee, J.-W. Park, Y. Gao, T. Lu, F.N. Egolfopoulos, D.F. Davidson, R.K. Hanson, C.T. Bowman, and H. Wang. A physics-based approach to modeling real-fuel combustion chemistry – IV. HyChem Modeling of Combustion Kinetics of a Bio-derived Jet Fuel and Its Blends with a Conventional Jet A. *Combust. Flame*, 198:477–489, 2018.

[34] N. Zettervall, C. Fureby, and E.J.K. Nilsson. A reduced chemical kinetic reaction mechanism for kerosene-air combustion. *Fuel*, 269:117446, 2020.

[35] Zettervall, N. *Methodology for developing reduced reaction mechanisms, and their use in combustion simulations*. PhD thesis, Department of Physics, Lund University, Lund, 2021.

[36] K. Kumar, C.-J. Sung, and X. Hui. Laminar flame speeds and extinction limits of conventional and alternative jet fuels. *Fuel*, 90:1004–1011, 2011.

[37] C. Liu, W.S. McGivern, J.A. Manion, and H. Wang. Theory and Experiment of Binary Diffusion Coefficient of n-Alkanes in Dilute Gases. *J. Phys. Chem. A*, 120:8065–8074, 2016.

[38] L. Zheng, R. Boylu, J. Cronly, I. Ahmed, E. Ubogu, and B. Khandelwal. Experimental study on the impact of alternative jet fuel properties and derived cetane number on lean blowout limit. *Aeronaut. J.*, 126:1997—2016, 2022.

[39] H. Versteeg and W. Malalasekera. *An Introduction to Computational Fluid Dynamics*. Prentice Hall, Harlow, 2007.

[40] N. Peters. *Turbulent Combustion*. Cambridge Monographs on Mechanics. Cambridge University Press, Cambridge, 2000.

[41] H.H. Chiu, H.Y. Kim, and E.J. Croke. Internal group combustion of liquid droplets. *Symp. (Int.) Combust.*, 19:971–980, 1982.

[42] M. Tanahashi, M. Sato, M. Shimura, and T. Miyauchi. DNS and Combined Laser Diagnostics of Turbulent Combustion. *J. Therm. Sci. Technol.*, 3:391–409, 2008.

[43] V. Papapostolou, D.H. Wacks, N. Chakraborty, M. Klein, and H.G. Im. Enstrophy transport conditional on local flow topologies in different regimes of premixed turbulent combustion. *Sci. Rep.*, 7:11545, 2017.

[44] R. Borghi. On the Structure and Morphology of Turbulent Premixed Flames. In C. Casci and C. Bruno, editors, *Recent Advances in the Aerospace Sciences*, pages 117–138. Plenum Press, New York, 1985.

[45] H. Yamashita, M. Shimada, and T. Takeno. A numerical study on flame stability at the transition point of jet diffusion flames. *Symp. (Int.) Combust.*, 26:27–34, 1996.

[46] S.B. Pope. Ten questions concerning the large-eddy simulation of turbulent flows. *New J. Phys.*, 6:35, 2004.

[47] C. Fureby and F.F. Grinstein. Monotonically Integrated Large Eddy Simulation of Free Shear Flows. *AIAA J.*, 37:544–556, 1999.

[48] H. Wu, P.C. Ma, and M. Ihme. Efficient time-stepping techniques for simulating turbulent reactive flows with stiff chemistry. *Comput. Phys. Commun.*, 243:81–96, 2019.

[49] F. Charlette, C. Meneveau, and D. Veynante. A power-law flame wrinkling model for LES of premixed turbulent combustion Part I: non-dynamic formulation and initial tests. *Combust. Flame*, 131:159–180, 2002.

[50] W.P. Jones and S. Navarro-Martinez. Large eddy simulation of autoignition with a subgrid probability density function method. *Combust. Flame*, 150:170–187, 2007.

[51] B.F. Magnussen. On the Structure of Turbulence and Generalized Eddy Dissipation Concept for Chemical Reactions in Turbulent Flow. In *Proceedings of the 19th Aerospace Sciences Meeting*, St. Louis, 12–15 January, 1981. AIAA 1981-0042.

[52] J. Chomiak. A possible propagation mechanism of turbulent flames at high Reynolds numbers. *Combust. Flame*, 15:319–321, 1970.

[53] E. Giacomazzi, C. Bruno, and B. Favini. Fractal modelling of turbulent combustion. *Combust. Theory Model.*, 4:391–412, 2000.

[54] V. Sabelnikov and C. Fureby. LES combustion modeling for high Re flames using a multi-phase analogy. *Combust. Flame*, 160:83–96, 2013.

[55] D.B. Spalding. A Single Formula for the "Law of the Wall". *J. Appl. Mech.*, 28:455–458, 1961.

[56] W.-W. Kim and S. Menon. A New Dynamic One Equation Subgrid-scale Model for Large Eddy Simulations. In *Proceedings of the 33rd Aerospace Sciences Meeting and Exhibit*, Reno, 9–12 January, 1995. AIAA 1995-356.

[57] A. Yoshizawa and K. Horiuti. A Statistically-derived Subgrid-scale Kinetic Energy Model for the Large Eddy Simulation of Turbulent Flows. *J. Phys. Soc. Jpn.*, 54:2834–2839, 1985.

[58] E. Quadarella, A. Péquin, A. Stagni, A. Parente, T. Faravelli, and H.G. Im. A generalized partially stirred reactor model for turbulent closure. *Proc. Combust. Inst.*, 39:5329–5338, 2023.

[59] G.M. Faeth. Mixing, transport and combustion in sprays. *Prog. Energy Combust. Sci.*, 13:293–345, 1987.

[60] J.K. Dukowicz. A Particle-Fluid Numerical Model for Liquid Sprays. *J. Comp. Phys.*, 35:229–253, 1980.

[61] C.T. Crowe. *Multiphase Flows with Droplets and Particles*. CRC Press LLC, Boca Raton, 1998.

[62] R.D. Reitz and R. Diwakar. Structure of High-Pressure Fuel Sprays. *SAE Trans.*, 96:492–509, 1987.

[63] B. Zuo, A.M. Gomes, and C.J. Rutland. Modelling superheated fuel sprays and vaporization. *Int. J. Engine Res.*, 1:321–336, 2000.

[64] W.E. Ranz and W.R. Marshall. Evaporation from drops. *Chem. Eng. Prog.*, 48:141–146, 1952.

[65] P.J. O'Rourke. *Collective drop effects on vaporizing liquid sprays*. PhD thesis, Los Alamos National Laboratories, Los Alamos, 1981.

[66] E. Hairer and G. Wanner. *Solving Ordinary Differential Equations*, chapter II: Stiff and Differential-Algebraic Problems. Springer, Berlin/Heidelberg, 1 edition, 1991.

[67] H. Jasak, H. Weller, and A. Gosman. High resolution NVD differencing scheme for arbitrarily unstructured meshes. *Int. J. Numer. Methods Fluids*, 31:431–449, 1999.

[68] N.W. Bressloff. A parallel pressure implicit splitting of operators algorithm applied to flows at all speeds. *Int. J. Numer. Methods Fluids*, 36:497–518, 2001.

[69] H.G. Weller, G. Tabor, H. Jasak, and C. Fureby. A tensorial approach to computational continuum mechanics using object-oriented techniques. *Comp. Phys.*, 12:620–631, 1998.

[70] P.W. Agostinelli, D. Laera, I. Boxx, L. Gicquel, and T. Poinsot. Impact of wall heat transfer in Large Eddy Simulation of flame dynamics in a swirled combustion chamber. *Combust. Flame*, 234:111728, 2021.

[71] W.P. Jones, A.J. Marquis, and K. Vogiatzaki. Large-eddy simulation of spray combustion in a gas turbine combustor. *Combust. Flame*, 161:222–239, 2014.

[72] A.H. Lefebvre. Airblast atomization. *Prog. Energy Combust. Sci.*, 6:233–261, 1980.

[73] C. Pichler and E.J.K. Nilsson. Pathway Analysis of Skeletal Kinetic Mechanisms for Small Alcohol Fuels at Engine Conditions. *Fuel*, 275:117956, 2020.

[74] T. Zeuch, G. Moréac, S. S. Ahmed, and F. Mauss. A comprehensive skeletal mechanism for the oxidation of n-heptane generated by chemistry-guided reduction. *Combust. Flame*, 155:651–674, 2008.

[75] J.C. Massey, I. Langella, and N. Swaminathan. Large Eddy Simulation of a Bluff Body Stabilised Premixed Flame Using Flamelets. *Flow Turbul. Combust.*, 101:973–992, 2018.

[76] G. Berkooz, P. Holmes, and J.L. Lumley. The Proper Orthogonal Decomposition in the Analysis of Turbulent Flows. *Annu. Rev. Fluid Mech.*, 25:539–575, 1993.

[77] J. Bae, S. Chaudhuri, P. Canteenwalla, and S. Yun. Combustion characteristics of sustainable aviation fuels in a scaled-down afterburner test rig. *Aeronaut. J.*, 128:1429–1449, 2024.

Scientific publications

Summaries and contributions

Co-authors are abbreviated as follows:
Arvid Åkerblom (AÅ), Christer Fureby (CF), Niklas Zettervall (NZ), Martin Passad (MP), Alessandro Ercole (AE), Elna Heimdal Nilsson (EN).

Paper I: Large Eddy Simulations of Turbulent Premixed Bluff Body Flames Operated with Ethanol, n-Heptane, and Jet Fuels

This paper describes the methodology and setup used for case A. The results include a fuel-dependent mesh sensitivity study, validation against experimental data, and a thorough comparison of ethanol, n-heptane, Jet A, and C1.

AÅ conducted the study and wrote the article. CF supervised, reviewed, and acquired funding.

Paper II: Comparing Chemical Reaction Mechanisms for Jet Fuel in Turbulent Premixed Combustion Simulations

This paper describes the working principles behind the compact Z79 and Z74 reaction mechanisms. These are then tested in case A with Jet A, JP-5, C1, C5, ethanol, and n-heptane. Each fuel is also simulated with a reference mechanism from the literature. A regression analysis identifies the global temperature ratio between reactants and products as the dominant factor for the overall flame size, both between fuels and between mechanisms for a given fuel.

AÅ conducted the LES study and wrote the majority of the article. NZ developed the Z79 and Z74 reaction mechanisms, ran simulations of laminar flames and auto-ignition, and

wrote two sections of the article. CF supervised, reviewed, and acquired funding.

Paper III: LES Modeling of the DLR Generic Single-Cup Spray Combustor: Validation and the Impact of Combustion Chemistry

This paper lays the foundation for subsequent studies of case B. The methodology is described, and the sensitivity of the results to the mesh resolution, (conventional) fuel choice, and turbulence-chemistry interaction model are gauged. The results are validated against experimental data, and the thermoacoustics of the case are investigated.

AÅ conducted the study and wrote the article. CF designed the mesh, supervised, reviewed, and acquired funding.

Paper IV: Numerical Modeling of Chemical Kinetics, Spray Dynamics, and Turbulent Combustion Towards Sustainable Aviation

This paper focuses on thoroughly describing Jet A, JP-5, C1, and C5. It is the broadest study in the thesis, with substantial portions dedicated to the composition of the fuels, their ignition characteristics, and their thermodynamic properties. A novel set of liquid property correlations are proposed and tested in case B. The simulation setup is developed further based on the findings in paper III. The paper closes with a general outlook on alternative jet fuels in aviation research.

AÅ developed the liquid model, conducted the LES study, and wrote the majority of the article. MP conducted the laminar flame study and wrote the associated section. NZ conducted the auto-ignition study and wrote the associated section. AE performed a literature survey and wrote the outlook section. CF designed the LES mesh, supervised, reviewed, and acquired funding. EN supervised, reviewed, and acquired funding.

Paper V: LES Modeling of the DLR Generic Single-Cup Spray Combustor: Comparison of Exploratory Category C Jet Fuels

This paper further develops the simulation setup for case B based on the findings in papers III and IV. The combustion of Jet A, C1, and C5 is explored in detail at both idle and cruise conditions. The liquid properties (particularly the vaporizability) are found to have a significant impact on the results, affecting the flame shape, mean mixture fraction, emissions, and the amplitude of the thermoacoustic oscillations.

AÅ conducted the study and wrote the article. CF designed the mesh, supervised, reviewed, and acquired funding.